

UCLA

UCLA Electronic Theses and Dissertations

Title

Novel Tunable Filters and Directional Filters for Modern Multiplexing Applications

Permalink

<https://escholarship.org/uc/item/7mv952hh>

Author

Sun, Shih-Peng

Publication Date

2013

Peer reviewed|Thesis/dissertation

UNIVERSITY OF CALIFORNIA

Los Angeles

Novel Tunable Filters and Directional Filters for Modern Multiplexing
Applications.

A dissertation submitted to in partial satisfaction of the
requirements for the degree Doctor of Philosophy
in Electrical Engineering

by

Shih-Peng Sun

2013

ABSTRACT OF THE DISSERTATION

Novel Tunable Filters and Directional Filters for Modern Multiplexing
Applications.

by

Shih-Peng Sun

Doctor of Philosophy in Electrical Engineering

University of California, Los Angeles, 2013

Professor Tatsuo Itoh, Chair

As the varieties of wireless services increase nowadays, selecting one of the service the user is targeting for becomes important. To do so, there are two popular methods, to use a tunable filter to dynamically select the service wanted, or to build a multiplexer capable of separating signals from different services to different channel for processing. Each method has its difficulties.

For tunable filters, the tuning frequency range seldom exceeds 2:1. This value is the ratio of the highest frequency the filter can be tuned to to the lowest. This means it can only select services within 2:1 frequency range. Also, as the filter is tuned to different frequency, its bandwidth usually varies as well.

Thus in the first two chapters, we first investigate a low-profile tunable filter structure that can be stacked vertically. By doing so, we can create a compact tunable filter bank. By switching to different tunable filters in the filter bank, we can cover the service in different frequency range. In Chapter 2, we describe a tunable filter, of which the bandwidth variation can be maintained small over the tunable filter tuning frequency range. The scheme to achieve this is simple and can be iteratively optimized numerically, which is very computationally efficient.

Multiplexer usually cannot be tuned. However, signal of each service may occupy different bandwidth at different frequency. Multiplexer can cater its response to each service it targets to, since a filter is dedicated to each service.

Directional filter is one of the multiplexing methods. Its main advantage is to enable a complex multiplexer system to be designed module by module. However, the directional filter structures existing in the literature are either too simple to support a good filtering response or has a manufacturing tolerance too tight to be practical.

Thus, the latter half of this dissertation is dedicated to the investigation of a new method to directional filter design so that it can realize high performance filtering and has more relaxed manufacturing tolerance. The theory of this method, the effectiveness and limitations are investigated and discussed in detail in Chapter 3 through Chapter 6.

The dissertation of Shih-Peng Sun is approved

Yuanxun Wang

Oscar Stafsudd

Katsushi Arisaka

Tatsuo Itoh, Committee Chair

University of California, Los Angeles

2013

Table of Content

CHAPTER 1	Compact Stackable Tunable Filter Bank	1
1.1	Introduction	2
1.2	Theoretical Analysis	5
1.2.1	Equivalent Circuit for Partially Shielded Split-ring Resonator	5
1.2.2	Parametric Study of the Step-impedance tunable resonator	7
1.3	Partially Shielded Tunable Filter Prototype	11
1.4	Stacking Tunable Filter Bank	17
1.5	Conclusion	21
1.6	Bibliography	22
CHAPTER 2	Tunable Filter with Simple Scheme to Maintain Absolute Bandwidth	24
2.1	Introduction	24
2.2	Filter Analysis	27
2.3	Prototype Development	30
2.4	Conclusion	35
2.5	Appendix: Iterative Optimization Algorithm	36

2.6	Bibliography	37
 CHAPTER 3 New Directional Filter--Background and Motivation ..38		
3.1	Bibliography	46
 CHAPTER 4 BRF-based Directional Filter -- Proof of Concept48		
4.1	Introduction.....	48
4.2	Concept of New Directional Filter Structure	49
4.3	Band-Reject Filter for New Directional Filter	51
4.4	New Directional Filter Prototype.....	53
4.5	Conclusion	55
4.6	Bibliography	56
 CHAPTER 5 Theory and Improvement of the BRF-based Directional Filter Structure.....57		
5.1	Introduction.....	57
5.2	Theory of BRF-based Directional Filter	59
5.3	Design of Differential BRF for Elliptical Directional Filter.....	63
5.4	Three-pole Elliptic Directional Filter Prototype	67
5.5	Isolation Improvement using CRLH Transmission Line.....	71
5.6	Conclusion	78

5.7	Bibliography	79
-----	--------------------	----

CHAPTER 6 Compact 4-pole BRF-based Directional Filter with Even-mode Matching Circuit for Sharp Cut-off.....82

6.1	Introduction.....	82
6.2	4-pole BRF Design	84
6.3	4-pole Directional Filter Prototype	87
6.4	Conclusion	90
6.5	Bibliography	90

List of Figures

Figure 1.1	The top view (a) and the stack-up profile (b) of the proposed partially shielded split-ring tunable filter structure.	3
Figure 1.2	A schematic of the partially shielded split-ring resonator.	5
Figure 1.3	The equivalent circuit for all the odd (a) and even (b) resonant modes.	6
Figure 1.4	Capacitance range to realize the tuning range from 380 MHz to 850 MHz with $Z_2 = 80 \text{ Ohm}$ and $2(\theta_1 + \theta_2) = 65 \text{ degree}$	7
Figure 1.5	The normalized frequencies of the first even spurious mode f_1 (a) and the first odd spurious mode f_2 (b) versus length ratio θ_2 / θ_1 at various impedance ratios K	8
Figure 1.6	The capacitance range and ratio (a) and the normalized spurious frequency f_1 (b) for the first even mode when the total length is varied.	10
Figure 1.7	The layout of the shielded prototype.	11
Figure 1.8	The coupling coefficient as the resonator is tuned to different center frequencies.	12
Figure 1.9	The simulated and measured S_{11} (a) and S_{12} (b) of the partially shielded split-ring tunable filter prototype.	14
Figure 1.10	The wideband simulation of the partially shielded split-ring tunable filter prototype, demonstrating a large spurious-free frequency region.	15
Figure 1.11	The measured P1dB (a) and IIP3 (b) of the developed tunable filter prototype. ...	16
Figure 1.12	Photograph of the developed partially shielded split-ring tunable filter prototype.	17
Figure 1.13	The 3D view of the tunable filter bank.	18

Figure 1.14	The measured S_{11} (a) and S_{21} (b) of the three filters in the tunable filter bank. ...	20
Figure 1.15	The photograph of the developed tunable filter bank prototype.	21
Figure 2.1	Topology of the proposed filter composed of a dual-mode resonator and input/output coupling inductors.	25
Figure 2.2	The circuit model of the equivalent resonator with extra loading introduced by input/output coupling.	27
Figure 2.3	The circuit model for the odd mode resonance (a) and the even mode resonance (b).	29
Figure 2.4	The desired and synthesized f_{even} and f_{odd} versus varactor capacitance.	31
Figure 2.5	The simulated filter response (a) and the bandwidth variation (b) across the tuning range.	32
Figure 2.6	The measured S-parameter (a) and the bandwidth (b) of the fabricated filter.	34
Figure 2.7	Photograph of the fabricated filter prototype.	35
Figure 2.8	Flow chart of the iterative optimization to find the proper input/output coupling inductance and position, and the perturbation stub lengths	36
Figure 3.1	Popular multiplexer structures other than directional filter, including (a) manifold-coupled multiplexer and (b) circulator coupled multiplexer.	38
Figure 3.2	The schematic and basic operation of a directional filter.	40
Figure 3.3	Three types of directional filters: the hybrid-coupled (a), the traveling-wave loop coupled (b), and $\lambda/2$ strip resonator coupled (c).	41
Figure 3.4	The differential (a) and common mode (b) excitation analysis of the $\lambda/2$ strip-resonator directional filter.	43

Figure 3.5	Two-stage directional filter consists of two identical single pole directional filter with 90° delay line (a), and its. typical coupled and through port responses (b)..	45
Figure 4.1	The proposed multiple-stage directional filter.....	49
Figure 4.2	The basic one-pole $\lambda/2$ strip-resonator directional filter.....	50
Figure 4.3	Microstrip layout for the differential BRF.....	51
Figure 4.4	Simulated S-parameters of the BRF compared with the ideal response.....	52
Figure 4.5	Photograph of the directional filter prototype based on the BRF in Figure 4.3....	53
Figure 4.6	Simulated and measured S-parameter of the directional filter in Figure 4.5.....	54
Figure 5.1	The basic structure of the BRF-based directional filter.....	60
Figure 5.2	The DF structure under common and differential excitations when the signal frequency is within the rejection bandwidth of the differential BRF.	61
Figure 5.3	The elliptic differential BRF that the directional filter prototype is going to be based on.	64
Figure 5.4	The response of the differential BRF in Figure 5.3 under differential (a) and common-mode (b) excitations.	66
Figure 5.5	The photo of the constructed BRF-based Directional Filter using the differential BRF in Figure 5.3.	68
Figure 5.6	The measured S-parameters of the three-pole elliptic directional filter prototype.	69
Figure 5.7	The S_{41} filtering response of the DF overlaid with S_{11o} of the differential BRF and the modified bound for S_{41} in practice.	70
Figure 5.8	The potential problem of a directional filter if isolation is poor.....	72

Figure 5.9	The photograph of the Directional Filter incorporating CRLH phase matching, and the realization of CRLH transmission line.....	73
Figure 5.10	The S-parameter (a) and the phase response (b) of the CRLH transmission.....	74
Figure 5.11	The $\Delta\theta$ comparison between the directional filter with and without the CRLH phase matching.....	76
Figure 5.12	The S-parameter response of the directional filter with CRLH phase matching, exhibiting high isolation.	77
Figure 6.1	The filter structure of the BRF (a) and the corresponding coupling matrix used in this work (b).....	84
Figure 6.2	The microstrip realization of the 4-pole BRF of Figure 6.1(a).....	85
Figure 6.3	BRF response from the coupling matrix (dotted) and the microstrip circuit (solid).	86
Figure 6.4	The realized DF prototype using the 4-pole BRF in Figure 6.2.	87
Figure 6.5	The simulated and measured S_{41} and S_{21} response of the DF prototype (a), and its measured matching and isolation performance (b).....	88

Vita:

Shih-Peng Sun came to the United States from National Taiwan University, Taiwan after he finished the Bachelor degree in 2006, and joined University of California, Los Angeles as a Master student. He spent seven years to finish M.S. and Ph.D. degree under the supervision of Professor Tatsuo Itoh.

In his master years, he focused on conformal retro-directive array and published two papers describing the synthesis and measurement of a prototype of a retro-directive array installed at the rounded nose of a small airplane. Right after he is awarded the M.S. degree, he spent the summer as an intern at Alcatel-Lucent Technology. There is mainly where he started the tunable filter works. He investigated and designed a stacked tunable filter bank as a compact and wide-band tunable filter solution. He published two papers in tunable filter area, the first one describing the stacked tunable filter bank, the other one describing a simple tunable filter structure that maintains the bandwidth when it is tuned to different frequencies. He started the research in directional filter in the latter half of his Ph.D. years. He has the honor to meet Humberto Lobato-Morales and Dr. Alonso Corona-Chavez, both visiting scholars from Mexico, and started the directional filter research together. Although later on their research branched into different directions, an enjoyable cooperative relationship is still maintained over the years. During his Ph.D. years, Shih-Peng Sun is also involved in projects about frequency scanning arrays, frequency selecting surface and small antenna.

He would like to particularly give appreciation to his parents who encouraged and supported him to come to U.S. for graduate studies, Professor Itoh for invaluable guidance and advises, and his knowledgeable and friendly colleagues in Microwave Electronics Lab, UCLA. Without any of them, he couldn't accomplish what he did.

CHAPTER 1

Compact Stackable Tunable Filter Bank

Nowadays, more and more wireless services are in development. Since different services are usually allocated at different frequencies, a tunable RF front-end that is capable of tuning to different wireless service is much desired. A crucial component of such a tunable RF front-end is tunable filter. However, obtaining the tuning range larger than 2:1 (ratio of frequency at the high end of tuning range to the low end frequency) is very difficult to achieve. In this chapter we propose and develop a partially shielded tunable filter structure using varactor-loaded split-ring resonator. The novel physical topology of the filter is suitable for vertical stacking of filters and enables a compact multi-layer tunable filter bank for applications requiring very wide tuning range. The capacitance range and ratio needed to achieve designated tuning range are presented and analytical solutions are given for the second and third higher-order modes to estimate the spurious free filter operation range. Two prototypes are developed. A partially shielded tunable filter using varactor-loaded split-ring resonators is developed to verify the design method and to demonstrate wide tuning range of a tunable filter. To further extend the tuning range, a filter bank with three stacked tunable filters at different frequency bands are designed and developed. With slight overlap between neighboring bands, a continuous tuning range of close to 5:1 is achieved.

1.1 INTRODUCTION

During the past years, various forms of tunable filters have been introduced [1.1]-[1.10]. Some tunable filter works focus on making the center frequency tunable [1.2]-[1.8], while some other interesting schemes have been developed to maintain the absolute BW of the filter throughout the tuning range [1.1], [1.9]-[1.10]. In [1.1], a complete theory for varactor loaded combline filter is presented. It is found that with an optimal length of the resonator, less than 20% variation in the passband bandwidth (BW) can be achieved with 2:1 tuning range. In [1.9] and [1.10], a ring-type structure and corrugated coupled lines are designed, respectively, to maintain the absolute BW of the bandpass filter within 10% variation. In this kind of tunable filters, varactor diodes are often used to make tunable resonators due to their fast response time and relatively high Q resonance. Some other more sophisticated tunable filters are reported in [1.11]-[1.13], capable of tuning both the center frequency and BW. To achieve this, more tunable or switching components are required and contribute to the higher insertion loss of the overall filter. Though tunable pre-select filters have received much attention in research community for decades, introducing wideband tunability in resonating electromagnetic structures with little or no loss in signal power and input nonlinearity remains technically challenging.

Despite the numerous studies previously done on tunable planar filters, to the authors' best knowledge, achieving center frequency tuning ratio larger than 2:1 with single tunable filter with reasonably low insertion loss remains very difficult. In this chapter, to bypass this difficulty, we investigate a structure that allows stacking multiple varactor-loaded split-ring resonator filters.

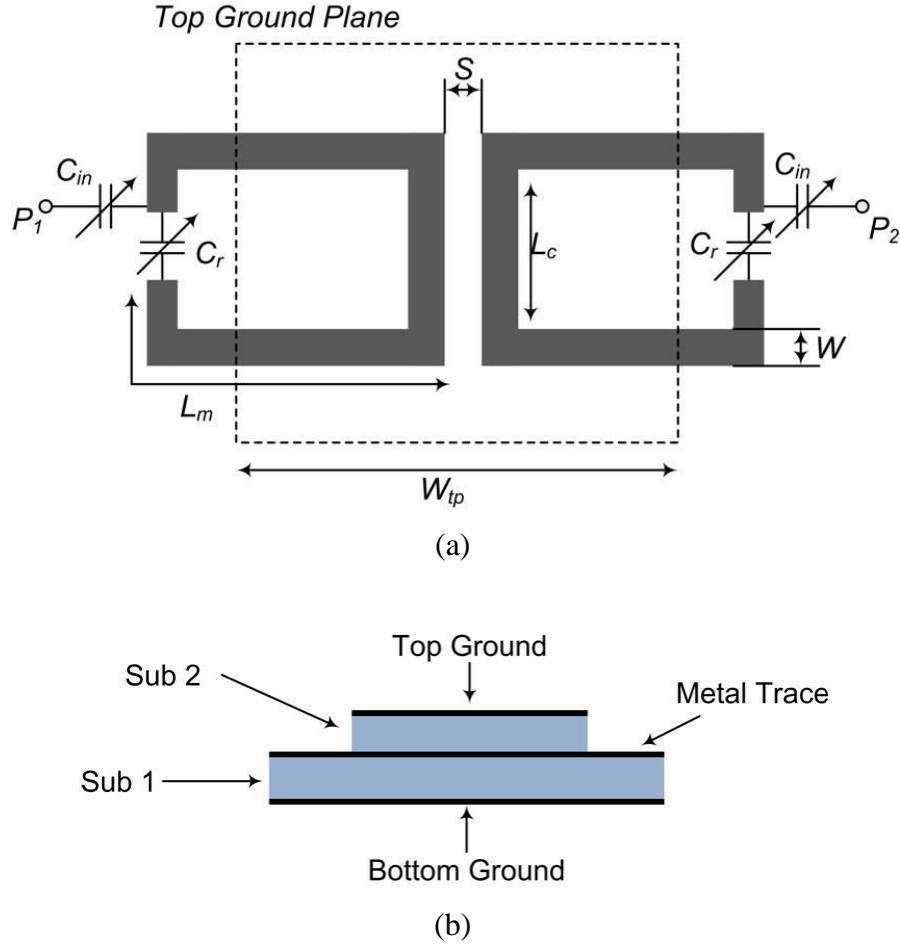


Figure 1.1 The top view (a) and the stack-up profile (b) of the proposed partially shielded split-ring tunable filter structure.

Such a stacking structure enables us to create a compact tunable filter bank that provides very wide frequency tuning range of close to 5:1. The basis of the proposed structure is a partially shielded split-ring tunable filter, and is illustrated in Figure 1.1. It is in principle the same as the split-ring tunable filter [1.5] except that in our proposed structure the central part is shielded by a top ground plane. Tunable capacitance C_r is responsible for the tuning of center frequency of the filter, and tunable capacitance C_{in} is used to achieve good impedance matching at different center frequencies. L_m , L_c , S and W represent physical dimension of various parts in the filter. Figure

1.1(b) shows the illustration of stack-up profile of the multi-layer structure of the filter. The two substrates Sub 1 and Sub 2 are usually of the same material and thickness.

The shielding of the top ground plane changes a portion of the microstrip line into the strip line that has different characteristic impedance and electrical length, thus modifying the resonator into a step-impedance split-ring resonator. The split-ring resonators and step-impedance resonators have been studied separately in the past in numerous literatures [1.5], [1.8], [1.10], [1.14]-[1.17]. However, the combination of the two, especially for the application to tunable filter, have not been reported yet. In this chapter, first the characteristics of the step-impedance split-ring tunable resonator, such as fundamental tunable resonance frequency and spurious frequencies, are studied carefully. A design procedure is proposed based on these studies, and a prototype is developed to verify the design procedure. Our prototype in this chapter deals with the case where the impedance changes across the boundary of two transmission lines by maintaining uniform line-width of the ring resonator. This results in smaller characteristic impedance for the strip-line portion. However, the study in this chapter can be easily extended to other cases, including the special case of changing the strip-line width such that the characteristic impedances of the two portions are the same.

After the study of a single shielded tunable filter prototype, we report a fully integrated tunable filter bank with three stacked tunable filters. Three filters are fabricated in a single multi-layer printed circuit board (PCB) fabrication process to form a single filter bank to cover a combined tuning range of 5:1.

1.2 THEORETICAL ANALYSIS

In this section, we will conduct parametric study for a partially shielded tunable split-ring resonator. The study covers important characteristics including fundamental resonance frequency, tuning range, and spurious response. These studies establish design process for tunable filters utilizing tunable split-ring resonators. A two stage tunable filter prototype is presented in the next section to validate parametric trend we established here.

1.2.1 Equivalent Circuit for Partially Shielded Split-ring Resonator

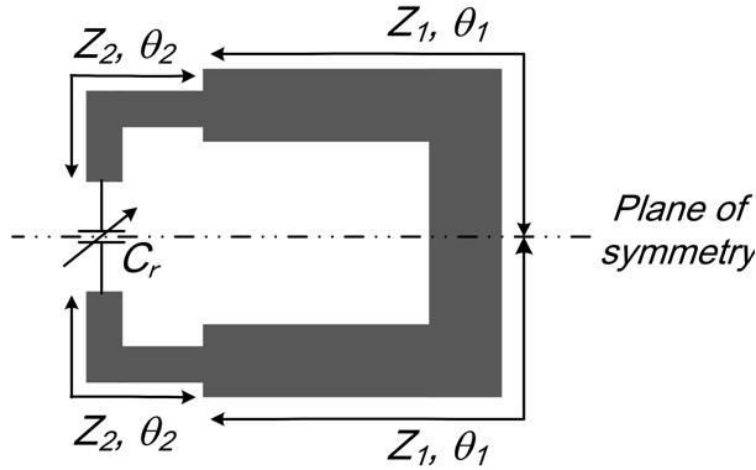


Figure 1.2 A schematic of the partially shielded split-ring resonator.

The resonator we employ in this development is the partially shielded split-ring resonator. The schematic of the resonator is shown in Figure 1.2, where Z_1 and Z_2 indicate characteristic impedance and θ_1 and θ_2 indicate electrical length of the transmission lines. Since the microstrip line in the shielded part becomes strip-line structure and has a characteristic impedance different from the unshielded part, it can be modeled as a step-impedance structure.

First we will study the fundamental resonance and the capacitance range needed for a pre-determined frequency tuning range. When the odd mode resonances occur, the Plane of

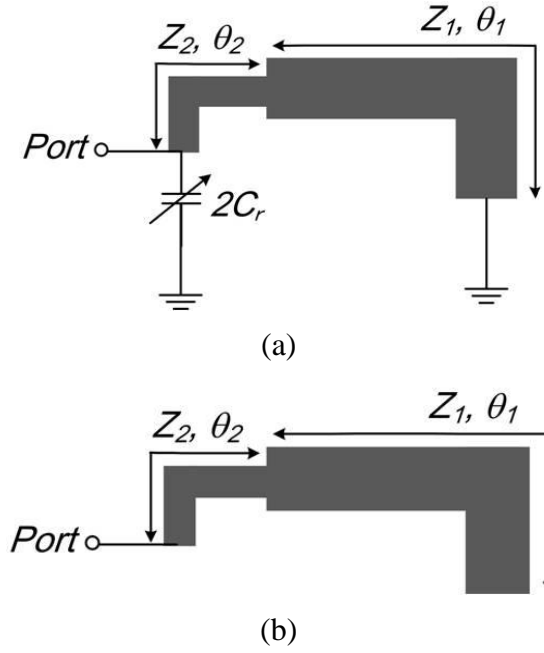


Figure 1.3 The equivalent circuit for all the odd (a) and even (b) resonant modes.

symmetry is short-circuited, and the equivalent circuit for all odd modes, including the fundamental mode, can be derived in Figure 1.3(a). Similarly, the equivalent circuit for all even mode resonances can be derived by replacing Plane of symmetry with open circuit, and is shown in Figure 1.3(b). The resonance condition for all the resonances is the input impedance looking into the Port to be infinity, and the condition for this to happen at odd and even resonances are derived in (1.1) and (1.2), respectively, using transmission line theory.

$$\frac{\cot \theta_1}{Z_1} = \frac{1}{Z_2} \frac{\tan \theta_2 + 2Z_2 \omega C_r}{1 - 2Z_2 \omega C_r \tan \theta_2} \quad (1.1)$$

$$Z_1 \cot \theta_1 = -Z_2 \cot \theta_2 \quad (1.2)$$

The characteristics of the resonator will be studied in the next section based on these two resonance conditions. One interesting fact that is worth noted is, while the characteristic of conventional SIR depends on the impedance ratio $K=Z_2/Z_1$ [1.14]-[1.17], in our case the actual value of Z_2 affects the fundamental resonance frequency in addition to the impedance ratio.

1.2.2 Parametric Study of the Step-impedance tunable resonator

For the purpose of studying the characteristic of this resonator, the tuning range is set to be 380 to 850 MHz, Z_2 is chosen to be 80 Ohm, and the total length of the transmission line $2(\theta_1 + \theta_2)$ to be 65° . We will summarize the characteristic of the resonator with this setup first, and then summarize the effect of varying the total length $2(\theta_1 + \theta_2)$.

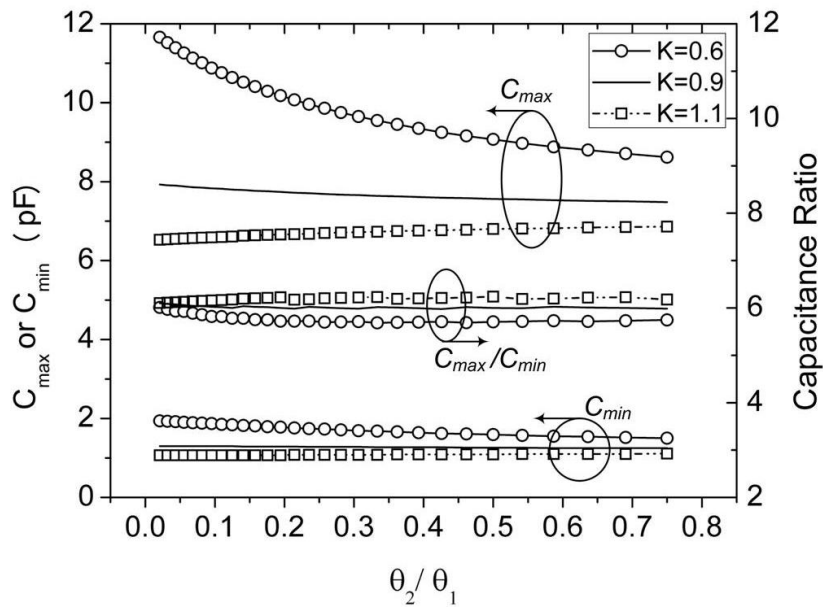


Figure 1.4 Capacitance range to realize the tuning range from 380 MHz to 850 MHz with $Z_2 = 80$ Ohm and $2(\theta_1 + \theta_2) = 65$ degree.

To determine the impedance ratio K and the length of each portion of the transmission line, we first study the required capacitance for our tuning range versus the length θ_2 . The required capacitance values C_{max} and C_{min} to tune the resonator to the two extremes of the tuning

range, i.e. 380 MHz and 850 MHz, respectively, are solved using (1.1) and plotted in Figure 1.4 with different K . The x-axis is the ratio θ_2/θ_1 , and the capacitance ratio C_{max}/C_{min} is also included in the plot. We can see that the capacitance value needed to achieve our tuning range decreases as K increases; however, the ratio of C_{max}/C_{min} is almost flat at 6 for all cases. For modern varactor technology, this ratio is very reasonable and commercially available.

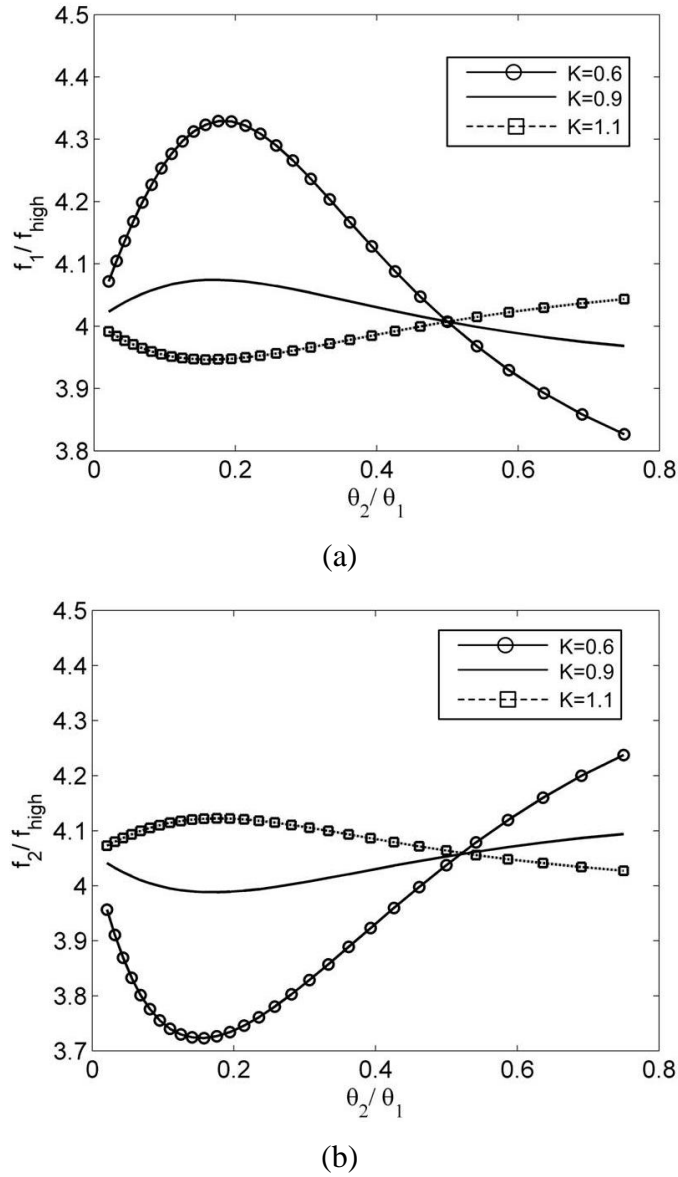
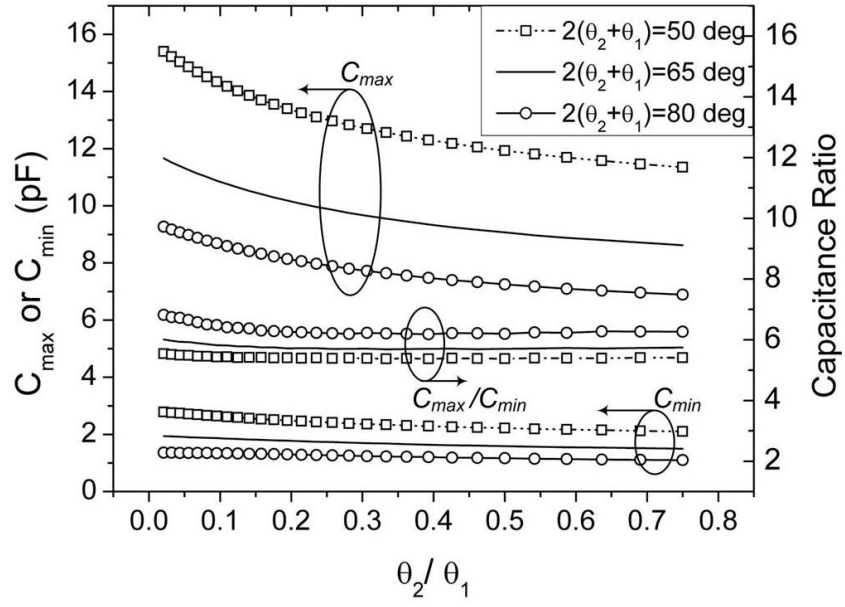


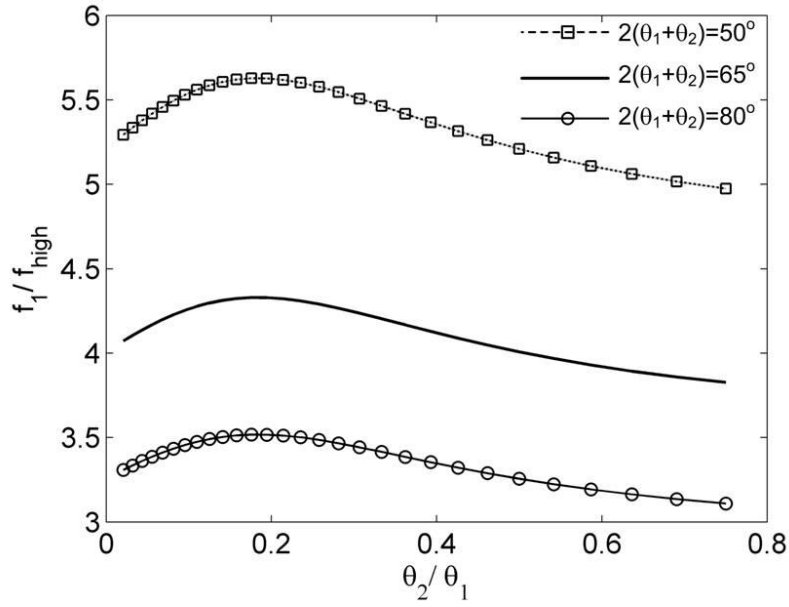
Figure 1.5 The normalized frequencies of the first even spurious mode f_1 (a) and the first odd spurious mode f_2 (b) versus length ratio θ_2/θ_1 at various impedance ratios K .

The resonance frequency of the first even spurious mode f_1 , and the first odd spurious mode f_2 are studied in Figure 1.5 (a) and (b), respectively, for different length ratio θ_2/θ_1 . In the figure, the two spurious resonance frequencies are normalized to f_{high} , which is the higher end of the frequency tuning range 850 MHz. Note that although f_1 is unaffected by C_r , f_2 is because it is an odd mode. Hence, the f_2 shown in the figure is when the C_r is tuned to C_{max} . This represents the lowest f_2 possible when the resonator is operating within the tuning range. We can see that although they vary slightly with K , they are all approximately 4 times higher than f_{high} . This is because the fundamental mode of this resonator is significantly lowered by the capacitance C_r .

We have seen the influence of K on the capacitor ratio and the spurious frequencies. However, these two characteristics are also affected by the total length of the resonator. In Figure 1.6(a), we show the capacitance ratio for $K=0.6$, but with different total length $2(\theta_1+\theta_2)$. The required capacitance value increases as the total length decreases. This is as expected since the transmission line portion acts as an inductive load for fundamental mode. The shorter the line, the smaller the inductance, and hence the larger capacitance is needed. However, the capacitance ratio is decreasing with increasing total length. This can be useful if high capacitance ratio varactor is not available while required tuning range stays the same. In Figure 1.6(b), we show the spurious frequency for the first even mode. The spurious frequency shifts to high frequency as the total length is reduced. Although only the even mode is shown, the odd mode spurious frequency follows the same trend providing good first order estimate of filter's spurious free operation range without full-wave simulations.



(a)



(b)

Figure 1.6 The capacitance range and ratio (a) and the normalized spurious frequency f_1 (b) for the first even mode when the total length is varied.

1.3 PARTIALLY SHIELDED TUNABLE FILTER PROTOTYPE

In this section, a prototype of the partially shielded tunable filter is developed based on the design graph and method introduced in the Chapter 1.2. Its performance is investigated and verified. Building on the success of this prototype, a stacking structure of multiple tunable filters will be introduced later.

The prototype is developed using 50 mil thick substrate with 3.7 relative permittivity for both layers of substrates in Figure 1.1. To begin, we choose Z_2 to be 80 Ohm for a reasonable line width in the microstrip portion. Since for this prototype, we want to keep the line width the same in both microstrip and strip line portion, the impedance ratio will be $K=0.69$. Based on Figure 1.4, the C_r for realizing the tuning range of 380 to 850 MHz is estimated to be 1.5pF to about 11pF. Based on Figure 1.5, the first spurious mode is at about 3.1 GHz even for the worst case scenario. The length ratio θ_2/θ_1 is then chosen to be 0.39 creating ample shielded area for additional stack-up filters in order to demonstrate the concept.

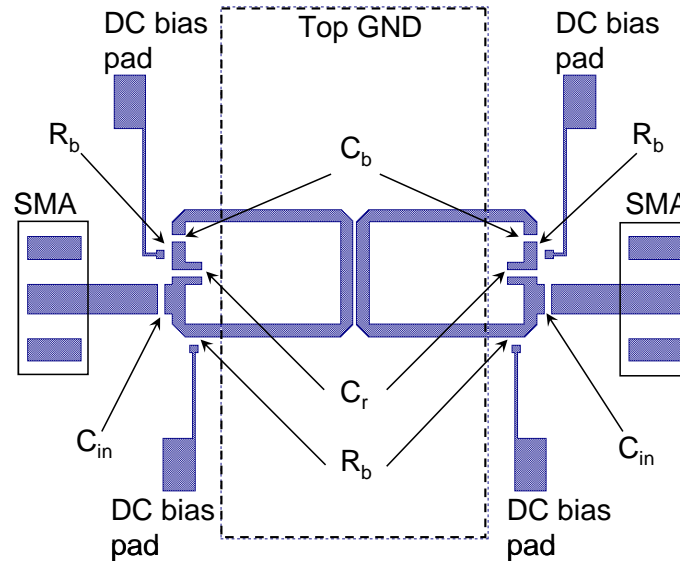


Figure 1.7 The layout of the shielded prototype.

Figure 1.7 shows the layout of the shielded prototype. Positions of various surface mount components are also marked out by arrows. C_r and C_{in} are varactors and are realized by mounting 2 different GaAs varactor diodes side by side. C_r is used to tune the center frequency of the filter, and C_{in} is tuned to maintain impedance matching at different center frequencies. C_b is the 100 pF chip capacitor used as DC block, preventing the transmission line from shorting the two DC bias voltages. The resistors R_b is 470k Ohm generic chip resistors from Panasonic. The huge resistance of R_b isolates the DC biasing circuits from the RF signal. Although in the DC bias path from the top bias pad to the bottom one there are two R_b resistors, the current flowing through the resistors are the leakage current of the varactor diodes under reverse bias and is very small. Hence the DC bias voltage can be applied to the varactor diodes with reasonable voltage

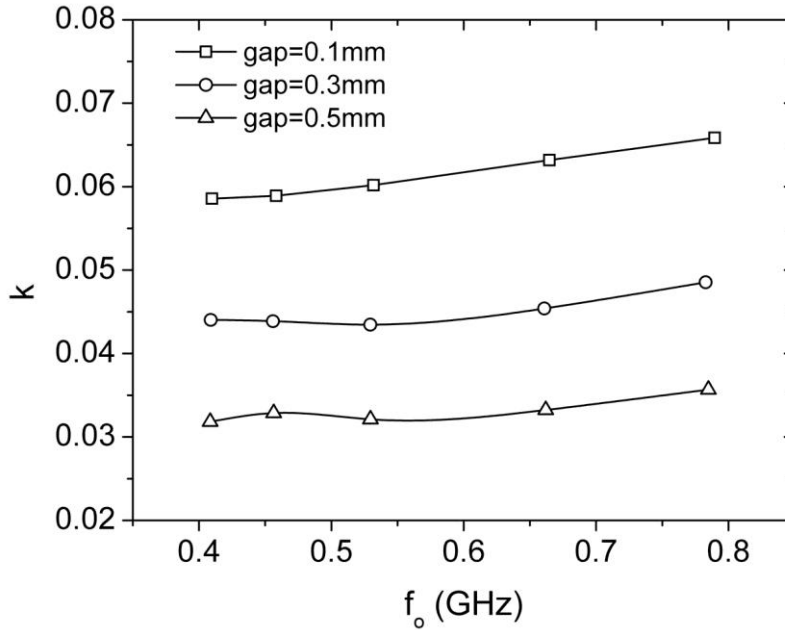
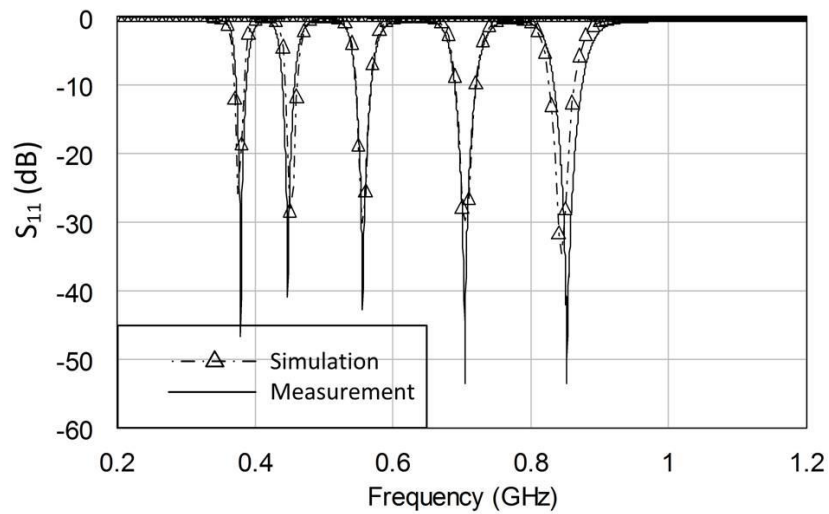


Figure 1.8 The coupling coefficient as the resonator is tuned to different center frequencies.

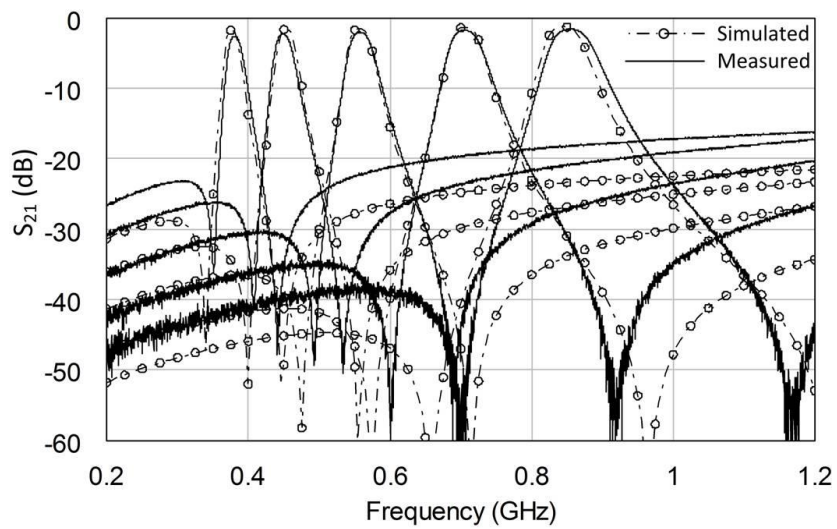
loss. The gap S is chosen so that the two resonators are coupled through a suitable coupling coefficient k , where k is defined as $(f_{\text{even}} - f_{\text{odd}})/f_o$, while f_{even} , f_{odd} are the resonant frequencies of

the coupled resonators [1.18]. The coupling coefficient k versus different center frequencies of tunable filters is plotted in Figure 1.8 with 3 different gap widths S . In the developed prototype, S is chosen to be 0.3 mm so that the FBW is about 6% in the center of the tuning range. The dimension of each part of the filter is, referring to variable definition in Figure 1.1, 9.6 mm for L_c , 18.35 mm for L_m , 0.3 mm for coupling gap S , and 25.1 mm for the width of the top ground plane. The width of the transmission line in the resonator is 1.2 mm, which results in 80.41 Ohm characteristic impedance for microstrip line portion and 55.1 Ohm for strip-line portion.

The filtering performance of the prototype is shown in Figure 1.9. Figure 1.9(a) shows the simulated and measured return loss S_{11} , and Figure 1.9(b) shows the simulated and measured insertion loss S_{21} . The full-wave simulation results through this work are obtained by method of moment based commercial software, Sonnet® together with lumped circuit models of varactor diodes. We can see that the two curves correspond to each other very well, except that the insertion loss is slightly lower in simulation. As C_r varies from 1.3 pF to 12 pF, the center frequency of the filter is tuned from 849MHz to 378MHz, which is pretty close to the design value. The corresponding value for C_{in} varies from 1.7 pF to 24 pF from the high to low end of tuning range. We can observe that as the center frequency is tuned, the transmission zero frequencies are also shifted and remain on both sides of the passband, which result in faster cut-off rate and provide a desirable feature. The insertion loss of this prototype is about 2.7dB at the lower end and 1.7dB at the higher end of tuning range. The difference of the insertion loss at the two ends of tuning range is related to the variation of fractional bandwidth (BW) and varactor Q . As can be observed in the figure, the fractional BW varies across the tuning range and is narrowest at the lower end (5.7%) and widest at the higher end (7.5%). Furthermore, to achieve



(a)



(b)

Figure 1.9 The simulated and measured S_{11} (a) and S_{12} (b) of the partially shielded split-ring tunable filter prototype.

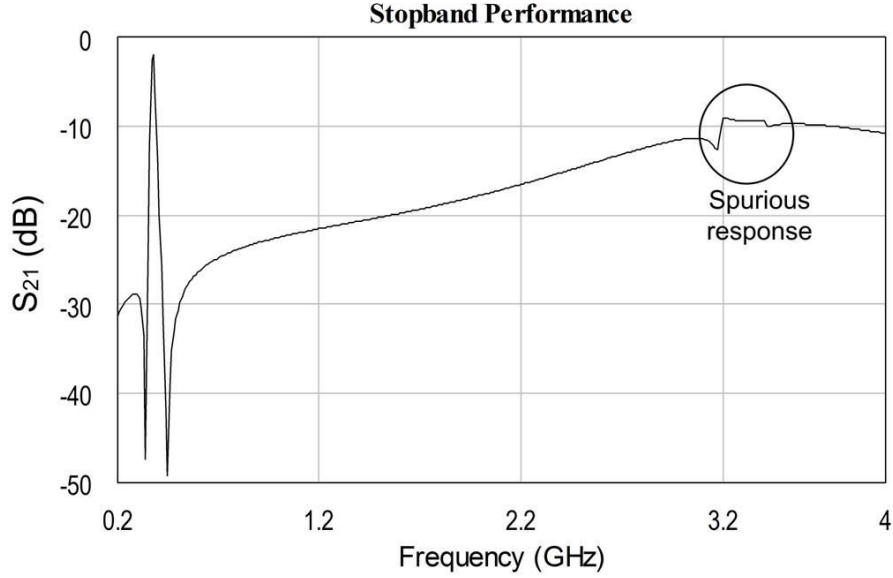


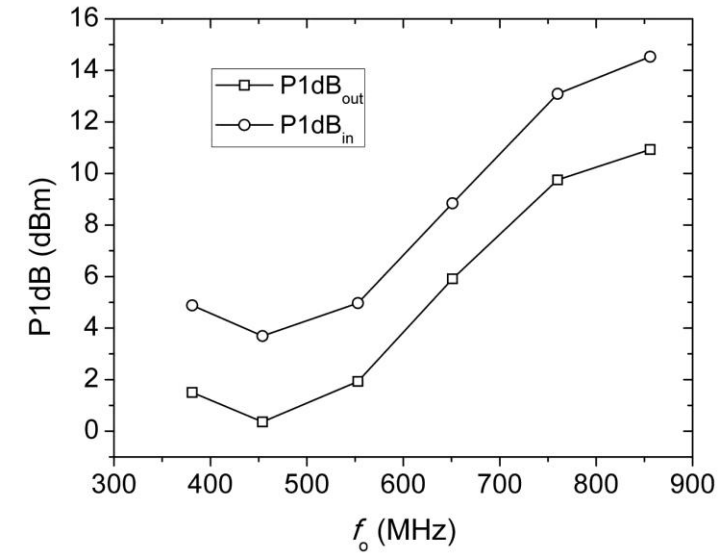
Figure 1.10 The wideband simulation of the partially shielded split-ring tunable filter prototype, demonstrating a large spurious-free frequency region.

tuning to lower center frequency, lower bias voltage needs to be applied, lowering Q of the varactor. Figure 1.10 shows the S_{21} of the filter from 0.2 to 4 GHz when tuned to 380 MHz. We can see that the spurious mode happens around 3.2 GHz, which corresponds with the prediction in the Section 1.2 very well, validating the accuracy and usefulness of analytical model.

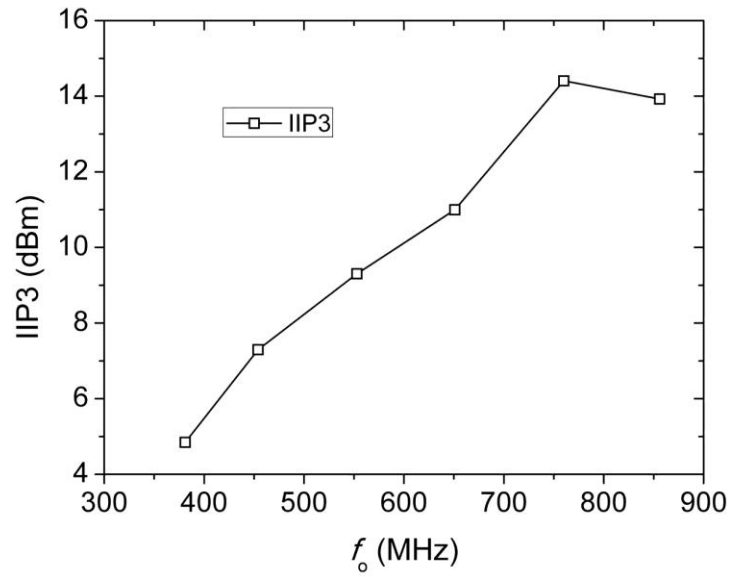
Linearity is an important metric because it shows how much the signal will be distorted when passing through the component. Since we introduce varactor components in the structure, the filter is expected to be nonlinear at certain input power, and its linearity performance is summarized in Figure 1.11. The measured input and output 1dB compression point (P1dB) and input 3rd order intercept point (IIP3) of the constructed prototype are shown in Figure 1.11(a) and (b), respectively. We can see a clear trend that, the linearity is better at higher end of the tuning range. This is because the varactor element tends to be more nonlinear at low bias condition when the filter is tuned to low center frequency. While the linearity of the developed tunable filter is limited by nonlinearity of GaAs varactor, the proposed filter topology is not

limited to the use with semiconductor varactors and is expected to have much improved linearity when combined with the MEMS varactors [1.9].

Lastly, the photograph of the developed prototype is shown in Figure 1.12.



(a)



(b)

Figure 1.11 The measured P1dB (a) and IIP3 (b) of the developed tunable filter prototype.

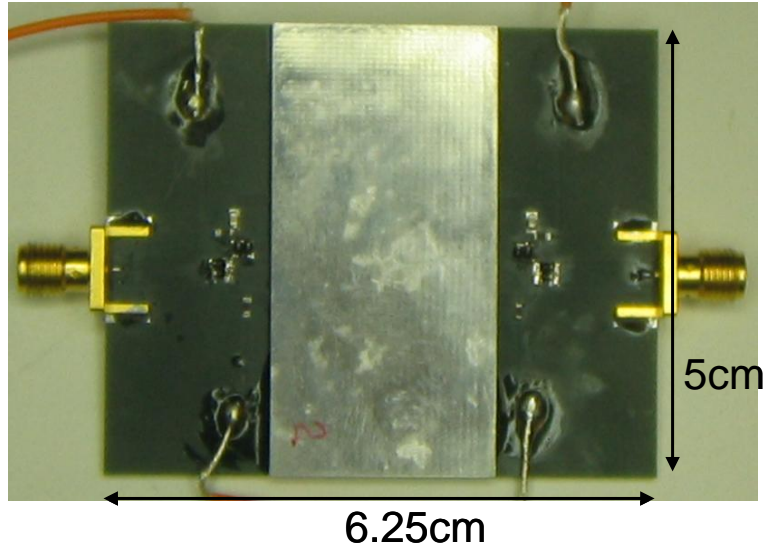


Figure 1.12 Photograph of the developed partially shielded split-ring tunable filter prototype.

1.4 STACKING TUNABLE FILTER BANK

Electronic tunable filter with wide tuning range exceeding over an octave is difficult to realize. We demonstrate in this section, the proposed novel structure of partially shielded tunable filter is capable in achieving aggregated wider tuning range by stacking multiple tunable filters on top of each other. Since we have to accommodate the surface mounted components, the top ground plane will be smaller than the whole size of the filter. Hence, the filter with higher center frequency should be naturally stacked on top of that with lower center frequency. Three tunable filters, having tuning ranges of 110 to 200MHz, 185 to 360MHz, and 350 to 530MHz respectively, are stacked on top of each other, forming a compact tunable filter bank. There is a slight overlap of the tuning range of each tunable filter to seamlessly cover the entire tuning range from 110 to 530MHz, corresponding to tuning range of close to 5:1.

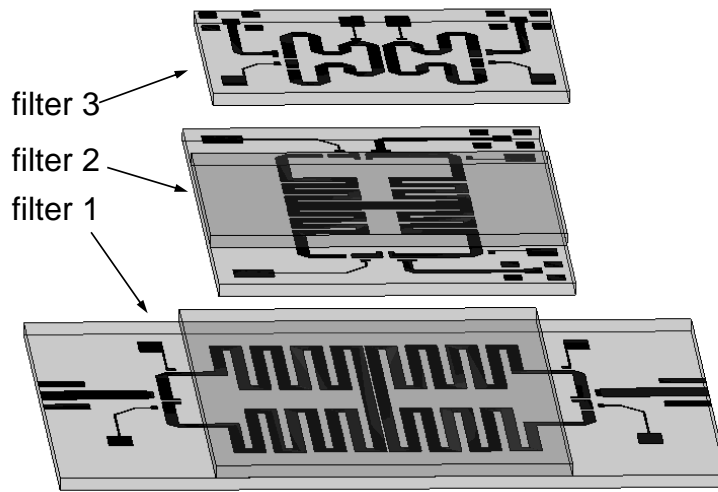


Figure 1.13 The 3D view of the tunable filter bank.

Figure 1.13 shows the 3D view of the three tunable filters that are stacked together. The filters are developed in one PCB fabrication process with multiple layers on single substrate material. The substrate layers and ground planes have been rendered partially transparent for a clear view of the structure.

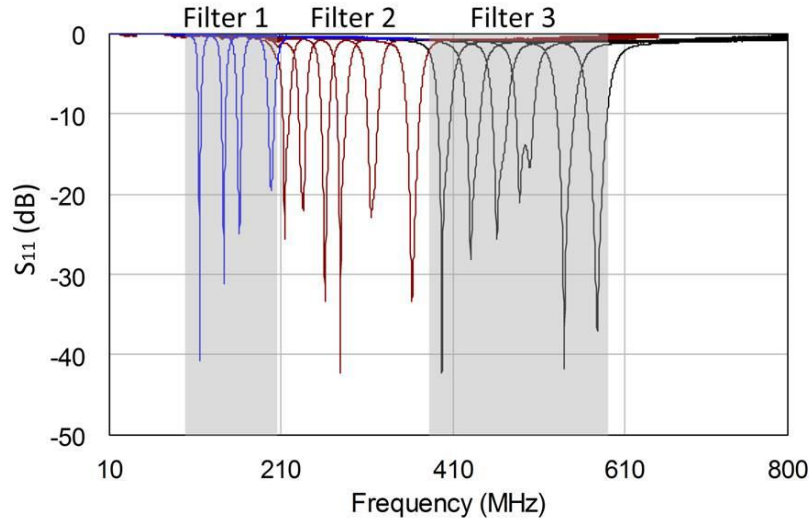
Filter one is the filter for the lowest band 110 to 200MHz. A substrate of 62mil thickness is used for both layers of substrate for this tunable filter. Although the detailed layout is not shown, it is understood that the structure is similar to the shielded prototype shown in Figure 1.7, and all the surface mount components are in place. The central part of the filter is shielded by another layer of substrate and the top ground plane. The tunable capacitance C_{in} and C_r are both realized by commercially available GaAs varactor diodes. The varactors are connected in parallel allowing the realization of capacitance up to 20pF before the biasing voltage drops below 4V. This gives us better insertion loss and linearity, since the loss and linearity of the varactor diode

tends to be poor under low biasing condition. All other surface mounted components in this tunable filter are the same as those in the shielded prototype introduced in the Section 1.2.

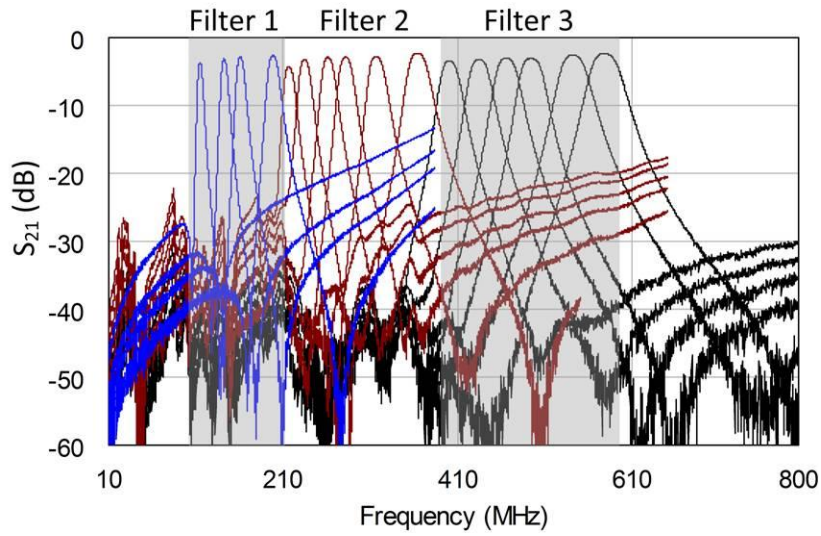
Filter two is the second tunable filter with tuning range of 185 to 360MHz. The capacitance C_r and C_{in} for this filter is realized the same way as in the first filter. Since the operating frequency is higher than that of the first filter and the capacitance is the same as the first filter, the transmission line part of the resonator is shorter. The whole structure can fit on the bottom ground plane that is the same size as the top ground plane of filter one, just as shown in Figure 1.13. Other surface mounted components are also the same except the vertically mounted SMA connector due to the space constraint.

For filter three, since the center frequency of this filter, 350 to 530MHz, is higher than the other two, less capacitance is needed for C_r . So C_r is realized with a single varactor diode, capable of tuning from 1.6 to 10pF for the biasing range 4 to 15V. All other surface mounted parts are the same as the other two filters, and the structure of the filter is similar to the other two except that since it is on the top most layers, no shielding is applied.

Figure 1.14 shows the measurement of insertion loss (S_{12}) of the three stacked prototypes. We can see that the frequency range of 110 to 530 MHz is seamlessly covered with the three tunable filters combined together. The measured insertion losses of the three filters are quite consistent with each other, and vary from about 4.2 dB at the lower end of each individual tuning range to about 2.4 dB at the higher ends. This decreasing trend of insertion loss also agrees with the single tunable filter prototype developed earlier. Within the tuning range of each filter, the fractional BW also varies. The variation of the fractional BW is similar for filter 1 and



(a)



(b)

Figure 1.14 The measured S_{11} (a) and S_{21} (b) of the three filters in the tunable filter bank.

2. It is found to be 4.6 to 6.4% from lower end to higher end of the tuning range for filter 1 and 2, and 5.5 to 6.2% for filter 3.

Figure 1.15 is the photograph of the stacked prototype. We can see that for this prototype, the input and output of the three tunable filters are separated, but it is imaginable that with

reasonable effort, a switching network can be realized to switch between the three filters and realize continuous tuning from 110 to 530MHz.

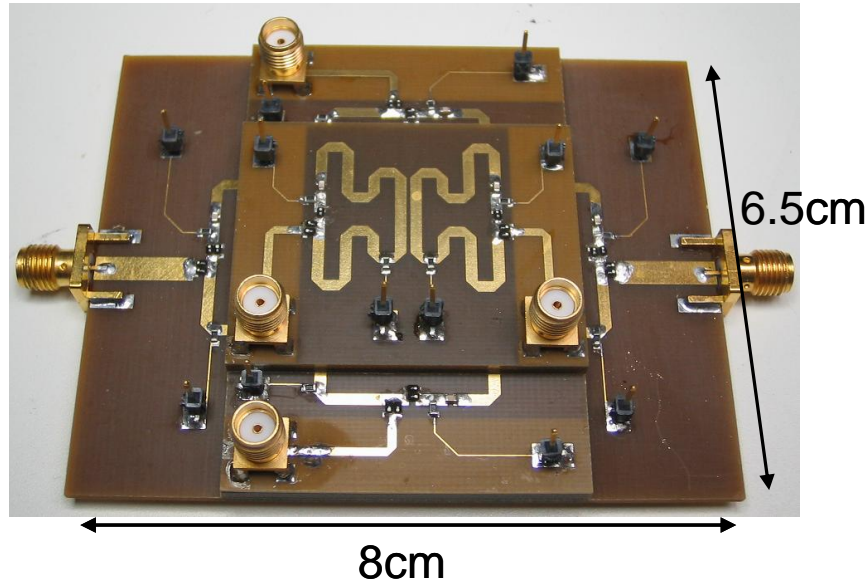


Figure 1.15 The photograph of the developed tunable filter bank prototype.

1.5 CONCLUSION

In this Chapter, we introduced a partially shielded split-ring tunable filter structure suitable for stacking multiple filters. This allows us to create a compact tunable filter bank to achieve very wide tuning range. The characteristic of this shielded split-ring resonator is studied carefully in this Chapter, including the spurious resonances. Although the spurious resonance frequencies depend on the details of the structure, a stopband range of 4:1 is predictable from the presented theoretical model.

A prototype tunable filter is developed using the proposed partially shielded structure, and the filter characteristics, tuning range and nonlinearity are investigated. With a single filter

structure, we achieve 2.25:1 tuning range with reasonable insertion loss in the passband and the measured results agree closely with the simulation. The spurious free range of about 3.7:1 is verified in the full-wave simulation, and agrees well with the theoretical study in Section 1.2. The insertion loss and the nonlinearity performance both improve as the center frequency is tuned to the higher end of the tuning range, and both are related to the characteristic of the varactor diodes under different bias condition.

Based on the success of the single partially shielded structure prototype, a filter bank prototype consisting of three tunable filters stacking on top of each other using the same partially shielded structure is developed. The filter bank has low profile, and, while preserving performance similar to the single partially shielded tunable filter prototype, the combined tuning range of close to 5:1 is achieved.

1.6 BIBLIOGRAPHY

- [1.1] I. C. Hunter and J. D. Rhodes, "Electronically tunable microwave bandpass filters," IEEE transaction on MTT, Vol. 30, no. 9, pp. 1354-1360, Sept. 1982.
- [1.2] I. C. Hunter and J. D. Rhodes, "Varactor tuned microwave filters," IEEE MTT-S Digest, pp. 399-401, 1982.
- [1.3] A. R. Brown, and G. M. Rebeiz, "A varactor tuned RF filter," IEEE MTT trans., vol. 48, no. 7, pp. 1157-1160, July 2000.
- [1.4] B.-W. Kim, and S.-W. Yun, "Varactor-tuned combline bandpass filter using step-impedance microstrip lines," IEEE MTT trans., vol. 52, no. 4, pp. 1279-1283, April 2004.
- [1.5] M. Makimoto, and M. Sagawa, "Varactor tuned bandpass filters using microstrip-line ring resonator," IEEE MTT-S Digest, pp. 411-414, 1986.
- [1.6] K. Chang, S. Martin, F. Wang, and J. L. Klein, "On the study of microstrip ring and varactor-tuned ring circuits," IEEE MTT trans., vol. 35, no. 12, pp. 1288-1295, Dec. 1987.

- [1.7] T. S. Martin, F. Wang, and K. Chang, "Theoretical and experimental investigation of novel varactor-tuned switchable microstrip ring resonator circuits," IEEE MTT Trans. Vol. 36, no. 12, Dec. 1988.
- [1.8] S. Kumar, "Electronically tunable ring resonator microstrip and suspended-substrate filters," Electronics letters, Vol. 27, issue 6, pp. 521-523, 1991.
- [1.9] Sang-June Park, and G. M. Rebeiz, "Low-loss two-pole tunable filters with three different predefined bandwidth characteristics," IEEE trans. MTT, Vol. 56, no. 5, pp. 1137-1148, May 2008.
- [1.10] M. A. El-Tanani, and G. M. Rebeiz, "Corrugated microstrip coupled lines for constant absolute bandwidth tunable filters," IEEE trans. MTT, Vol. 58, no. 4, pp. 956-963, 2010.
- [1.11] K. Kawai, H. Okazaki, and S. Narahashi, "Center frequency and bandwidth tunable filter employing tunable comb-shaped transmission line resonators and J-inverter," European Microwave Conference proceedings, pp. 649-652, 2006.
- [1.12] B. E. Carey-Smith, P. A. Warr, M. A. Beach, and T. Nesimoglu, "Wide tuning-range planar filters using lumped distributed coupled resonators," IEEE Trans. Microwave Theory Tech., vol. 53, no. 2, pp. 777-785, Feb. 2005.
- [1.13] K. Kawai, H. Okazaki, and S. Narahashi, "Center frequency, bandwidth, and transfer function tunable bandpass filter using ring resonator and J-inverter," European Microwave Conference proceedings, pp. 1207-1210, 2009.
- [1.14] S.-Y. Lee and C.-M. Tsai, "New cross-coupled filter design using improved hairpin resonators", IEEE Trans. Microw. Theory Tech., vol. 48, no. 12, pp.2482 -2490, 2000.
- [1.15] J.-S. Hong, and M. J. Lancaster, "Microstrip filters for RF/microwave applications," Wiley-Interscience publication, pp. 19-21.
- [1.16] M. Makimoto, and S. Yamashita, "Compact bandpass filters using stepped impedance resonators," Proc. IEEE, vol 67, pp. 16-19, Jan. 1979.
- [1.17] M. Makimoto, and S. Yamashita, "Bandpass filters using parallel coupled stripline stepped impedance resonators," IEEE MTT Trans., vol. 28, no. 12, Dec. 1980.
- [1.18] M. Sagawa, K. Takahashi, and M. Makimoto, "Miniaturized hairpin resonator filters and their application to receiver front-end MIC's," IEEE trans. MTT, vol. 37, no. 12, Dec. 1989.

CHAPTER 2

Tunable Filter with Simple Scheme to Maintain Absolute Bandwidth

A research focus on tunable filters other than wide tuning range is to maintain the bandwidth of the tunable filter while its center frequency is tuned. In particular, we are interested in maintaining the absolute bandwidth of the filter while it is tuned to different center frequency. In this Chapter, we present the realization of a constant bandwidth two pole tunable filter by means of dual mode resonance. The proposed filter has a simple bandwidth control scheme, making numerical optimization of the bandwidth variation across the tuning range possible. A prototype having tuning range of 0.85~1.4GHz using lumped inductors as input/output coupling elements has been realized. The bandwidth of the fabricated prototype varies between 51~59MHz across the tuning range and good matching is achieved within the whole tuning range.

Although we focus on maintaining the absolute bandwidth over the tuning range, it is clear that this methodology can also accommodate design of increasing and decreasing bandwidth over the tuning range of the tunable filter.

2.1 INTRODUCTION

Tunable filter has been a hot topic of research for more than three decades, and can be roughly categorized into mechanically tuned, electronically tuned, and YIG filters. In recent years, electronically tuned filters, especially varactor diode tuned filters, have been receiving a

lot of attention due to its swift tuning capability and the advent of high Q GaAs varactor diodes [2.1].

Among various performance considerations regarding the tunable filter, bandwidth (BW) variation control has remained to be highly concerned, and achieving constant absolute BW over the tuning range is desired. In [2.1], Hunter and Rhodes showed that this can be achieved by the proper selection of the length of the resonators in varactor loaded comb-line filter topology. Theoretically it can achieve BW variation less than 20% within an octave tuning range. Further modification is done by Kim and Yun in [2.2] for microstrip implementation, and more precise BW control was achieved. Even more complete BW control capability is demonstrated by Park *et al* in [2.3] by means of controlling independent electric and magnetic coupling.

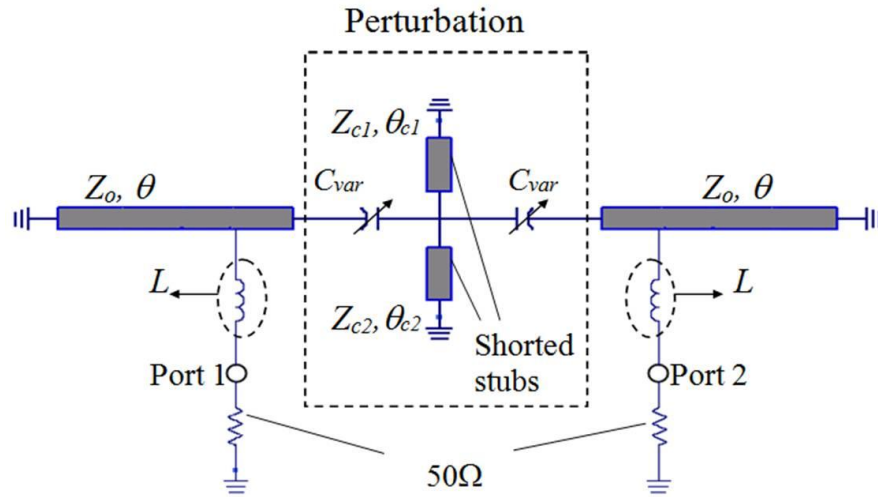


Figure 2.1 Topology of the proposed filter composed of a dual-mode resonator and input/output coupling inductors.

In this Chapter, we present another approach to maintain the absolute BW of the filter over the tuning range. This approach is easy to analyze and provides an alternative to the comb-line approach in [2.1]. The dual-mode resonance has been widely studied in the literature. It is known that it can be achieved by introducing perturbation in the resonator and is a compact

structure for realizing a two-pole bandpass filter [2.4][2.5]. In Figure 2.1 we show the topology of the proposed tunable filter realized by dual-mode resonance. The ports 1 and 2 are the filter input and output ports, and the signal entered into the port is coupled into or out of the resonator through coupling inductors. The choice of inductive coupling helps us to obtain better upper stopband rejection.

As shown, we introduce two parts of perturbation into a half-wavelength shorted end resonator. The varactor part is included in the perturbation to achieve tuning of the center frequency of the filter, and the two shorted stubs of the perturbation control the amount of difference in the odd and even resonance frequencies, and this separation is related to the BW of the filter. As we tune the varactor capacitance value, the resonance frequency of the resonator changes, as well as its impedance slope versus frequency. To maintain a constant absolute BW, the two shorted stubs must provide a frequency dependent perturbation to match the change of the resonator impedance slope over the tuning range. The optimized stubs structure that achieves this, as well as the input/output coupling inductance and position, are selected by an iterative algorithm, which is detailed in Section 2.5.

To build such a two-pole filter from a dual-mode resonator, the loading introduced by the input/output coupling inductors has to be considered carefully. In [2.5], it is demonstrated that this loading effect influences both resonance modes and introduces unwanted deviation in the prescribed BW, resulting in devastating effect on the BW control. In Section 2.2, this effect is also taken care of before the resonator analysis.

Based on the analysis we present in Section 2.2, a dual-mode resonance tunable filter prototype is developed for tuning range of 0.85~1.4 GHz in Section 2.3, and is implemented in microstrip form. Fabrication and measurement results are summarized lastly in Section 2.4.

2.2 FILTER ANALYSIS

From Figure 2.1, we see that the filter is composed of two parts, the resonator and the coupling structure. It is known in the filter design that because a single series inductor is different from the ideal admittance inverter, it will introduce extra loading to the dual-mode resonator and influence the resonance properties. Hence, the equivalent resonator which includes this extra loading must be found before the analysis for the resonator can take place. This equivalent resonator is shown in Figure 2.2, where X is the reactance realized by the pair of shunt shorted stubs in parallel, and B is the susceptance of the extra loading introduced by the input/output coupling inductor. The amount of the extra loading B is presented in (2.1), where L

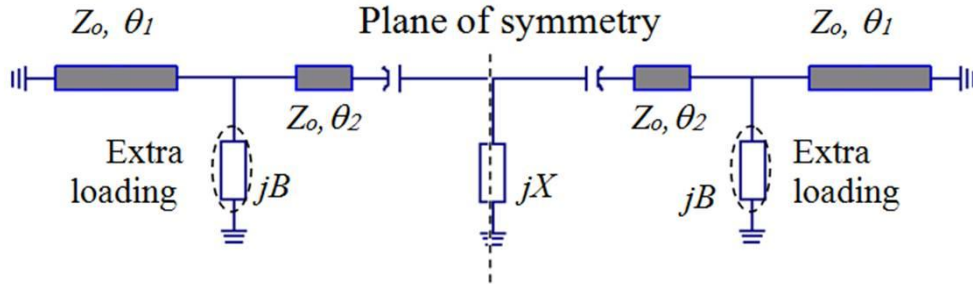


Figure 2.2 The circuit model of the equivalent resonator with extra loading introduced by input/output coupling.

$$B = \frac{1}{\omega L(1 + G^2 \omega^2 L^2)} - \frac{1}{\omega L} \quad (2.1)$$

is the value of the input/output coupling inductance, and G is equal to 0.02, which is the conductance of the 50 Ohm port termination.

There are two modes of resonance for this equivalent resonator in Figure 2.2, namely the odd and even modes. At odd mode resonance, the plane of symmetry is short circuited and the equivalent circuit model is shown in Figure 2.3(a). At even mode resonance, the plane of symmetry becomes open circuited and the equivalent circuit model is shown in Figure 2.3(b). In even mode equivalent circuit, a factor of 2 is added to the shunt reactance X because when dividing the circuit into two halves under even mode resonance, the shunt reactance jX in Figure 2.2 must first be divided into two shunt reactance of $j2X$ in parallel. The resonance conditions for odd and even modes are presented in (2.2) and (2.3) respectively, where C_{var} is the capacitance of the varactor, and Y_L is the admittance shown in Figure 2.3 and can be calculated through simple transmission line analysis.

$$j\omega C_{var} = -Y_L \quad \text{at } f=f_{\text{odd}} \quad (2.2)$$

$$2X - \frac{1}{\omega C_{var}} = -\frac{1}{jY_L} \quad \text{at } f=f_{\text{even}} \quad (2.3)$$

$$k = \frac{2|\Delta f|}{f_{\text{odd}} + f_{\text{even}}} = \frac{BW}{f_o \sqrt{g_1 g_2}} \quad (2.4)$$

Comparing Figure 2.3(a) and (b), we can see that if X is small, the two resonance modes should be close to each other, and the amount of the difference between the two resonance frequencies $\Delta f=f_{\text{odd}}-f_{\text{even}}$ is controlled by the amount of X , namely the dimensions of the stubs. From the theory of coupled resonator filter, the separation of the two resonance frequencies Δf is related to the coupling coefficient k and the BW of the filter through (2.4) [2.5], where f_o is the

center frequency of the filter. Hence, the BW variation of the realized tunable filter across the tuning range can be controlled simply by choosing the appropriate stub configuration.

In particular, once the desired BW and tuning range of the center frequency f_o are decided, we can calculate the desired odd and even resonance frequencies as $f_{\text{odd}} = f_o + 0.5\Delta f$ and $f_{\text{even}} = f_o - 0.5\Delta f$.

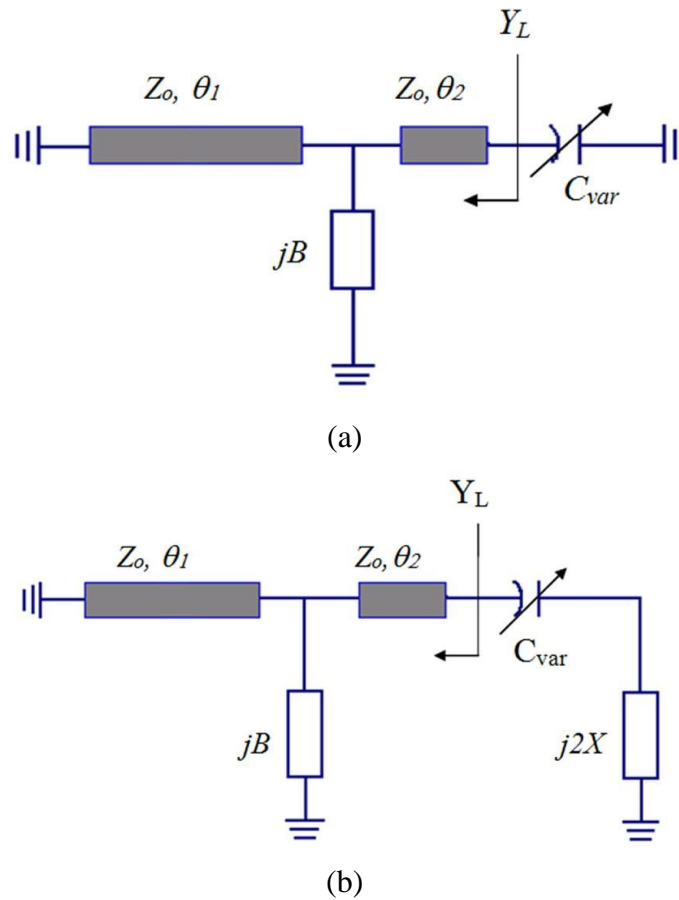


Figure 2.3 The circuit model for the odd mode resonance (a) and the even mode resonance (b).

Then from (2.2), the capacitance range needed can be obtained, and from (2.3) the desired shunt reactance X can be found. Once this desired reactance is known, we can find the optimal stub configuration by an exhaustive search within the solution space with reasonable

stub dimensions for minimum mean square error (MMSE) solution with respect to the desired X . This is demonstrated in the next section.

2.3 PROTOTYPE DEVELOPMENT

A dual-mode resonance filter prototype with tuning range of 0.85~1.4 GHz is developed based on the analysis in the previous section to validate the concept. The goal of the BW control is to obtain constant absolute BW over the tuning range. We assume the TL part of the resonator to have $Z_o=75$ Ohm and $\theta=42^\circ$. Differing from the conventional filter design, the construction starts from specifying the input position and input/output coupling inductance first. Since the series coupling inductance is a type of lowpass circuit, the upper stopband rejection would improve significantly over the capacitive input/output coupling case. For this prototype, inductance value of 24 nH is chosen.

After specifying the input inductance, the desired shunt reactance X can be found as previously mentioned once the desired absolute BW and the lowpass prototype have been specified. In this case, they are specified as 82.5 MHz and Butterworth prototype for demonstration.

As shown in Figure 2.1, a pair of shorted stubs is used to approximate the desired shunt reactance. The optimal stub dimensions can be found by performing an exhaustive search for minimum mean square error (MMSE) solution in the acceptable solution space. In particular, we limited the range of the characteristic impedances of the two stubs Z_{c1} and Z_{c2} to be 70~105 Ohm, and the range of the electrical length of the two stubs θ_{c1} and θ_{c2} to be $3^\circ\sim30^\circ$ for reasonable layout dimensions. Furthermore, $Z_{c1}=Z_{c2}$ is assumed for convenience. The exhaustive search only costs about a minute on a computer. After the stub structure is found, S_{11} response across the

tuning range is checked. This process is repeated until an input position that achieves acceptable matching is found.

For this prototype, a good input configuration is found with input position at 35.7° away from the shorted end of the resonator. Corresponding to this input configuration, the capacitance range is calculated to be about 1.3~4.5 pF, and the optimal stub dimensions are $Z_{c1}=Z_{c2}=97$ Ohm, and $\theta_{c1}=\theta_{c2}=4^\circ$.

Figure 2.4 shows the ADS simulated f_{even} and f_{odd} compared to the desired one. We can see that the simulated f_{odd} follows the desired one almost exactly, but f_{even} fluctuates somewhat around the desired value. This is because in the design methodology, the capacitance for a certain f_{odd} can be realized exactly, while the desired shunt reactance for f_{even} can only be approximated by MMSE solution. The maximum deviation from desired f_{even} is observed to be 7.6 MHz at the lower end of frequency range, where the approximate reactance deviates from the desired one the most.

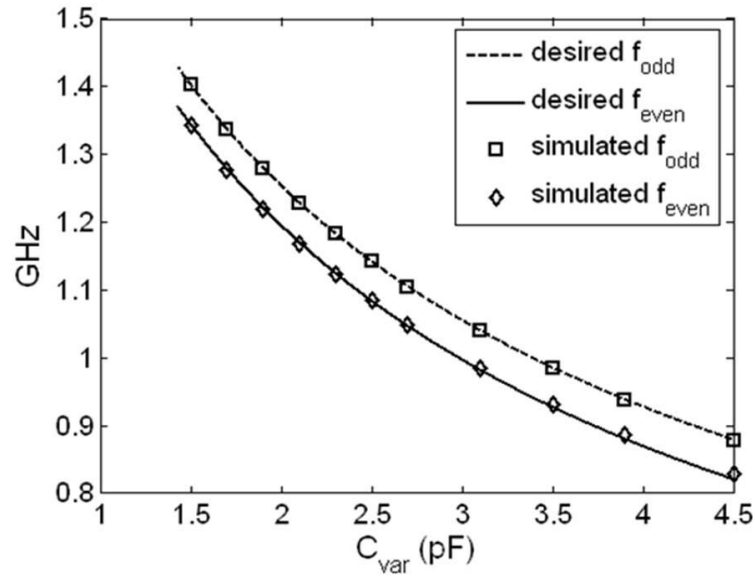
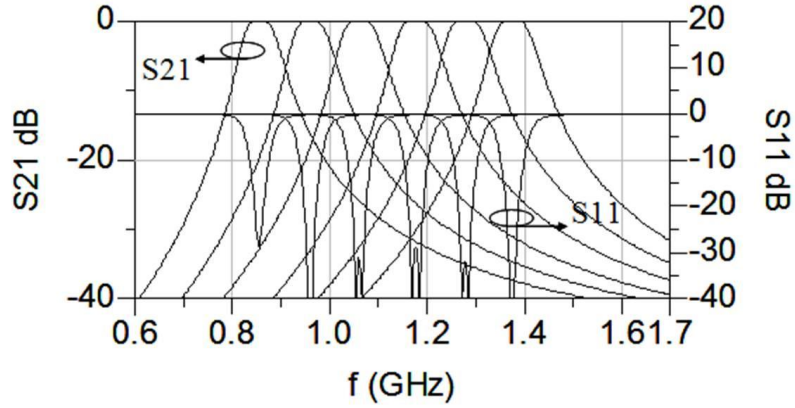
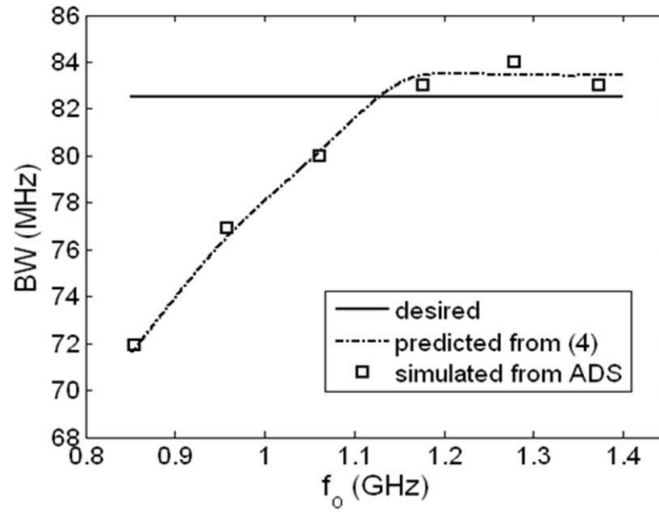


Figure 2.4 The desired and synthesized f_{even} and f_{odd} versus varactor capacitance.



(a)



(b)

Figure 2.5 The simulated filter response (a) and the bandwidth variation (b) across the tuning range.

The performance of the filter prototype synthesized is simulated by Agilent ADS and summarized here. Figure 2.5(a) shows the filter response within the whole tuning range. We can observe that the return loss is always lower than -25dB and approximates the maximally flat response reasonably well. Figure 2.5(b) summarizes the desired 3-dB bandwidth, the predicted 3-dB BW from (2.4), and the actual simulated BW. We can see that the predicted and the actual simulated bandwidth agree with each other pretty well. Furthermore, the realized BW deviates

from the desired one the most at the lower edge of the tuning range, and is about 11 MHz lower. This is in agreement with the observation that f_{even} deviates from the desired value the most at the lower edge of the tuning range. Better BW variation performance can be obtained by choosing other inductor value, or further optimization including more parameters such as Z_o and θ .

The prototype developed in the previous section is implemented in microstrip line configuration with 50 mil thick Rogers RT5880 substrate. Since all the electrical lengths of the lines are specified at frequency 1.1 GHz, the physical dimensions of the filter is translated to be 2 mm wide and 23.7 mm long for the transmission line in the resonator, and 1.2 mm wide and 2.28 mm long for both of the parallel stubs. However, due to the parasitic inductance associated with the shorting via, the length of the transmission line part of the resonator is tuned to a shorter length of 22.5 mm.

The varactors used in the implementation are MA46H072 GaAs based tuning diodes from M/A COM, and is specified in the data sheet to have tuning range of 1.3~8 pF from 20~0V bias voltage. Since chip capacitor with large capacitance tend to have larger loss and variation, two varactors with their cathodes connected to a common bias is used to realize a single tuning capacitor in the schematic, avoiding the use of DC block capacitor. The input/output coupling inductors are 22 nH air coil from Coilcraft, which, from the TRL calibration data, have inductance close to 24 nH in this frequency range.

The measured filter performance is summarized in Figure 2.6. In Figure 2.6(a) we show the S-parameter of the filter across the tuning range. Insertion loss of 3.85~4.2 dB is observed. This is partially due to the loss of the varactor and partially to the loss of coupling inductor. From the TRL calibration data, the loss of the inductor increased substantially in this frequency range. The frequency range is also down shifted. This is due to the parasitic package inductance

and capacitance of the varactors. Figure 2.6(b) shows the measured BW in the tuning range, and is observed to be 51~59 MHz for tuning frequency range of 0.78~1.38 GHz. Although the loss decreases the BW of the filter, the general trend is still observed to agree with Figure 2.5.

Figure 2.7 shows the photograph of the fabricated microstrip prototype of this tunable filter.

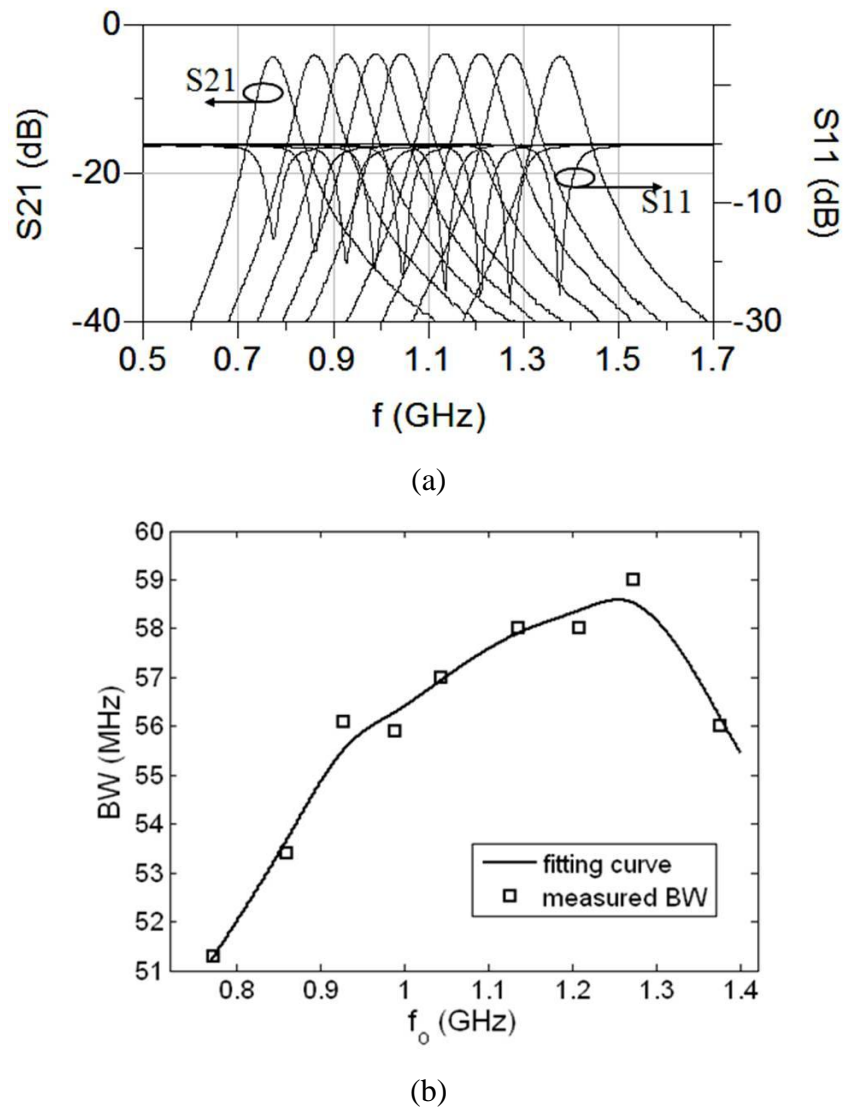


Figure 2.6 The measured S-parameter (a) and the bandwidth (b) of the fabricated filter.

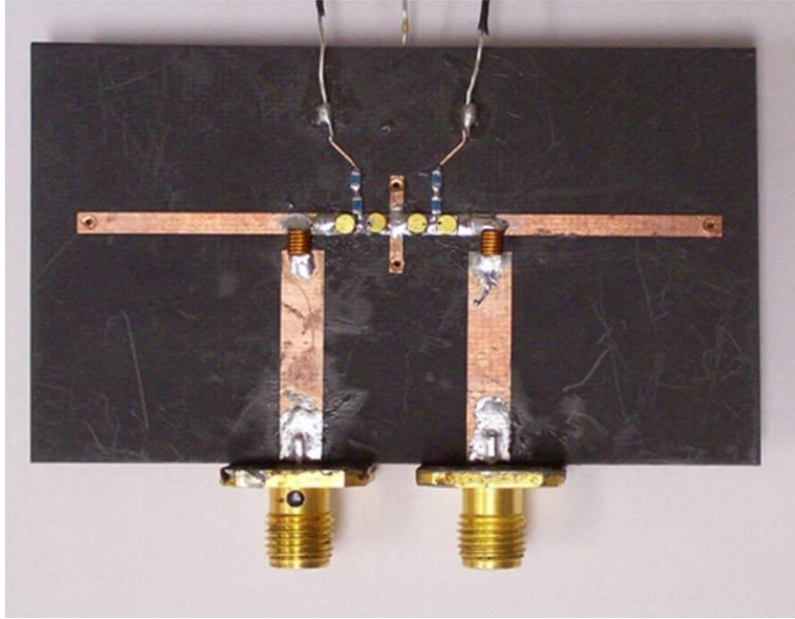


Figure 2.7 Photograph of the fabricated filter prototype.

2.4 CONCLUSION

In this Chapter, the concept of using dual-mode resonator to achieve BW control is presented. The theory agrees with the ADS circuit simulation very well, validating the concept and the synthesis methodology. The developed prototype has maximum BW variation about 13% with respect to the desired bandwidth, while in the fabrication, about 16% variation with respect of the narrowest BW is observed. Although input/output coupling is realized by a fixed value inductor, good matching is maintained in both simulation and implementation.

2.5 APPENDIX: ITERATIVE OPTIMIZATION ALGORITHM

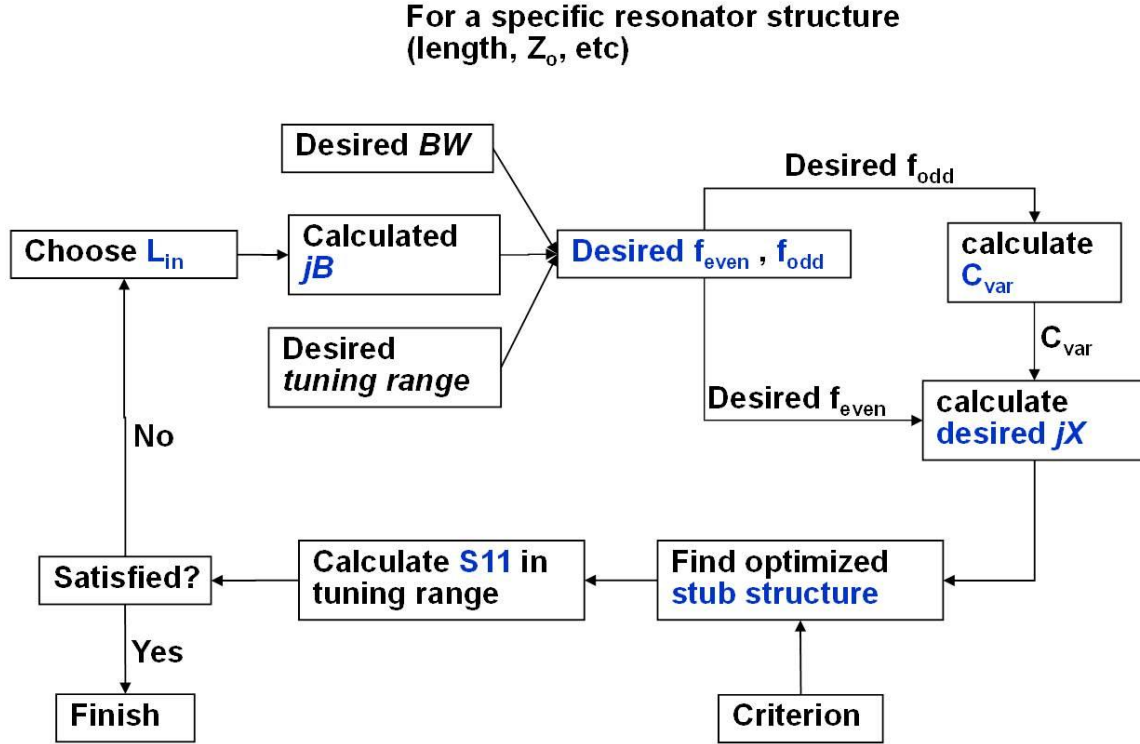


Figure 2.8 Flow chart of the iterative optimization to find the proper input/output coupling inductance and position, and the perturbation stub lengths

In Section 2.3 we mentioned the method of which the prototype design is based on. Here we present the flow chart of this design method for clearness. The flow chart is shown in Figure 2.8. Before starting the process described by this chart, we must decide on the Z_o and θ of the microstrip part of the resonators, as shown in Figure 2.1, since there are too many design parameters.

Using the specified Z_o and θ , this algorithm is capable of calculating the return loss responses of the tunable filter when tuned across the tuning range for a specified input/output coupling inductance L_{in} . If the result is not satisfactory, we sweep through available inductance value for L_{in} , until satisfactory responses are obtained across the tuning range. If after sweeping

through the available value of L_{in} but the responses are not satisfactory, then we need to change the Z_o or θ of the resonator and start again. As can be seen, this is a multi-dimensional searching process.

2.6 BIBLIOGRAPHY

- [2.1] I. C. Hunter, and J. D. Rhodes, "Electrically tunable microwave bandpass filters," IEEE Trans. Microwave Theory & Tech., vol. 30, no. 9, pp. 1354-1360, September 1982.
- [2.2] B.-W. Kim, and S.-W. Yun, "Varactor-tuned combline bandpass filter using step-impedance microstrip lines," IEEE Trans. Microwave Theory & Tech., vol. 52, no. 4, pp. 1279-1283, Apr. 2004.
- [2.3] S.-J. Park, and G. M. Rebeiz, "Low-loss two-pole tunable filters with three predefined bandwidth characteristics," IEEE Trans. Microwave Theory & Tech., vol. 56, no. 5, pp. 1137-1148, May 2008.
- [2.4] M. Matsuo, H. Yabuki, and M. Makimoto, "Dual-mode stepped-impedance ring resonator for bandpass filter applications," IEEE Trans. Microwave Theory & Tech., vol. 49, no. 7, pp. 1235-1240, July 2001.
- [2.5] A. C. Kundu, and I. Awai, "Effect of external circuit susceptance upon dual-mode coupling of a bandpass filter," IEEE Microwave and Guided Wave Letters, vol. 10, no. 11, pp. 457-459, Nov. 2000.

CHAPTER 3

New Directional Filter--Background and Motivation

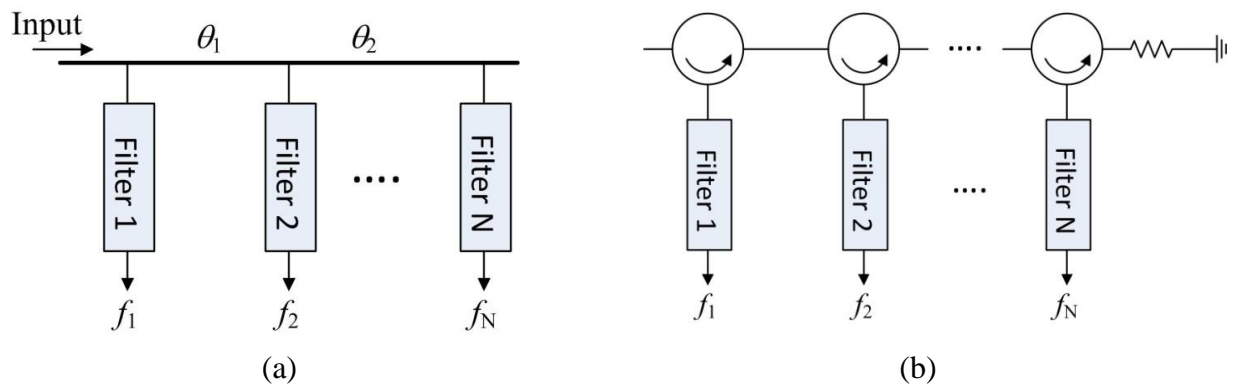


Figure 3.1 Popular multiplexer structures other than directional filter, including (a) manifold-coupled multiplexer and (b) circulator coupled multiplexer.

Nowadays, there are more and more wireless services with each wireless service occupying a unique frequency band. To support these demands, designing the circuits that can properly separate or combine signals occupying different frequencies has become crucial in the modern wireless communication. This process, called multiplexing, has been studied for decades. There are mainly three multiplexing structures that can accomplish the required tasks: manifold coupled multiplexer, circulator coupled multiplexer, and directional filter. The difference in these structures is the way they connect filters of different frequencies and the way they deal with the interaction between these filters [3.1].

The first two types of multiplexers other than directional filters are shown in Figure 3.1. The manifold multiplexers in Figure 3.1(a) directly connect different filters using transmission lines. The main advantage is low loss, since transmission lines are relatively lossless. For this reason, these types of multiplexers are popular at the output stage [3.1], preserving as much power output from the high-power power amplifier as possible. However, transmission lines do not provide adequate isolation between different filters, so the undesired interaction between the filters is very strong. The result of this strong interaction leads to a very complicated design process, since tuning or modifying the circuit for a specific channel filter will inadvertently alter the response of other channels as well. Therefore the design of the manifold multiplexers relies heavily on optimization [3.1], and the fine tuning of this multiplexer after it is manufactured presents a headache.

Shown in Figure 3.1(b) is the circulator-coupled multiplexer. This type of multiplexers is relatively easy to design. Since circulators provide good isolations between filters, there is minimum interaction between channels. Hence, one can use off-the-shelf filters without any modifications for the assembly of this multiplexer. However, the disadvantage is higher loss and expense due to circulators. Notice when the signal flows from one channel of the multiplexer to the next, it passes through two circulators. Thus the insertion loss for the successive stages accumulates quickly.

Directional filter can provide good isolation between different channels without using the circulator. Low interactions between the channels allow one to assemble a complex multiplexer by designing individual channels first and then cascading them together later. Loss and linearity performance of the multiplexer is also improved since circulators are not needed.

The basic schematic and operation of a directional filter is shown in Figure 3.2. The directional filter has four ports: input port, coupled port, through port, and isolation port. The input port (P1) is matched to 50 Ohm for a wide frequency range. Generally, a 100% impedance matching bandwidth can be demonstrated. The coupled port (P4) extracts only a specific designed frequency band from the input signal. That means the S-parameter S_{41} resembles that of the S_{21} of a bandpass filter response. The rest of the frequencies that are not extracted to P4 remain intact and emerge from P2, the through port. Thus the S-parameter S_{21} of the directional filter resembles that of a band-reject filter response, passing all the frequencies except the frequency band that was extracted to P4. This signal can be fed into the input port of the next directional filter to extract another frequency band. Thus, by connecting multiple directional filters in the cascaded fashion, we can extract different frequencies to different ports sequentially and build a multiplexer. P3 is the isolated port, and ideally there should be no signal coming out of P3 when the signal is input from P1.

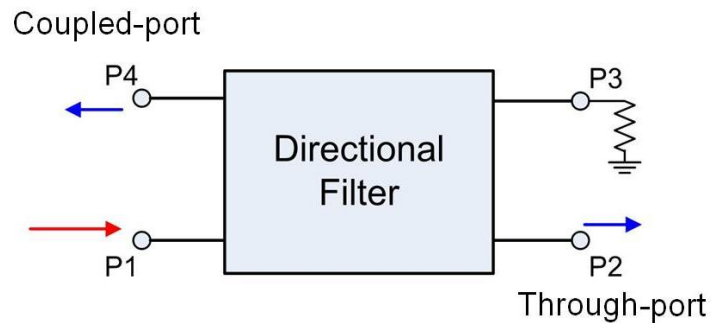


Figure 3.2 The schematic and basic operation of a directional filter.

There are three main types of directional filter, the hybrid-coupled directional filter, the traveling-wave loop coupled directional filter, and $\lambda/2$ resonator coupled directional filter. These are shown in Figure 3.3. The hybrid-coupled directional filters are shown in Figure 3.3(a), along

with the corresponding ports P1 through P4. It consists of two 90° -hybrid and two identical bandpass filters. The advantage of this structure is that the coupled-port response of S_{41} will resemble that of the bandpass filter used in the structure [3.2]-[3.4]. Thus it is relatively easy to design a directional filter with good filtering response by employing multi-stage bandpass filters inside the structure, of which the design method is well documented and experimented in the literature [3.5]-[3.10]. It is relatively easy to manufacture as well, since the circuitry used in the structure are all well-known and studied structures. However, 90° -hybrid makes the structure bulky and cumbersome, and the usable bandwidth of this directional filter structure is limited by the 90° hybrid.

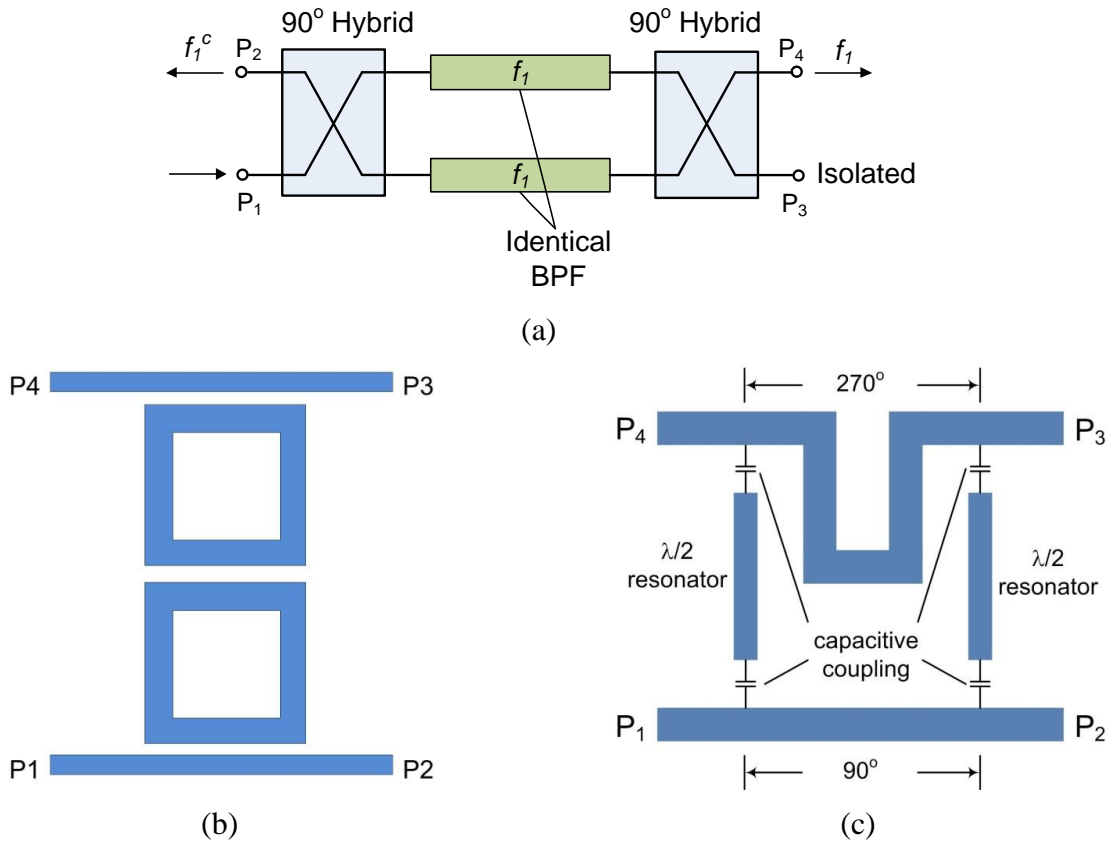


Figure 3.3 Three types of directional filters: the hybrid-coupled (a), the traveling-wave loop coupled (b), and $\lambda/2$ strip resonator coupled (c).

The loop-coupled directional filter is shown in Figure 3.3(b). The ports P1-P2 and P3-P4 are connected by the transmission lines. However, there are loops coupling to the two transmission lines. These loops are of the length 1λ at the center frequency of the directional filters. Thus, at the center frequency, the loops resonate, and the energy is coupled from port P1 to P4 [3.11]-[3.14]. By adding multiple loops, multi-pole directional filter structure can be realized. To be specific, the structure shown in Figure 3.3(b) is a two-pole directional filter. This structure is more compact when compared to the hybrid-coupled directional filter, but the drawback is that the loops in the structure are very sensitive to manufacturing defects. The reason is that the loop resonator in this structure acts differently from other resonators in the conventional filters. For example, when a conventional cavity resonator resonates there are two traveling waves with the same amplitude but going in opposite directions. However, in the loop resonator, there is only one traveling wave. To be specific, when the signal is input from P1, there is only clockwise traveling wave resonating inside the loop. Unfortunately, the directionality of the directional filter depends heavily on the purity of this traveling wave. Hence, any defects in the loop that sets up a reflection and creates another traveling wave in counter-clockwise direction will degrade the performance of the directional filter. The tight manufacture tolerance often makes the fabrication and tuning of this kind of directional filter expensive or even impractical [3.5].

The $\lambda/2$ strip-resonator directional filter has both compactness and robustness. It does not require additional 90° -hybrid circuit like hybrid-coupled directional filter, and its resonator is not a traveling wave type, thus has more relaxed manufacturing tolerance compared to loop-coupled directional filter.

The working mechanism of this type of directional filter can be visualized by analyzing the common and differential mode excitations between the ports P1 and P4 at the resonance frequency of the $\lambda/2$ strip resonators. If P1 and P4 are excited differentially, this differential signal will excite the first $\lambda/2$ strip-resonator it encounters, and reflects back to P1 and P4. This situation is depicted in Figure 3.4(a), where the voltage standing wave of the resonating mode of the resonator is also shown. Notice that the voltage at the two ends of the resonator is 180° out-of-phase, hence it can only be excited by differential signal on the transmission lines.

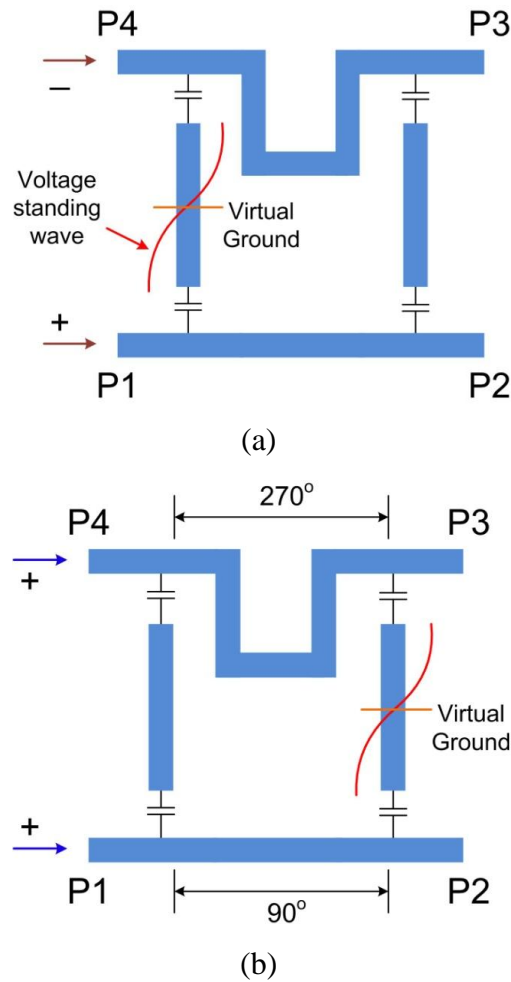


Figure 3.4 The differential (a) and common mode (b) excitation analysis of the $\lambda/2$ strip-resonator directional filter.

On the other hand, if P1 and P4 are excited with common mode excitation, the situation would be as shown in Figure 3.4(b). The common mode excitation will not excite the first resonator, since it is only excited by differential signal. However, after passing through the delay lines that has 180° phase difference, common mode excitation becomes differential mode and excites the second resonator and gets reflected. The two reflected modes illustrated in Figure 3.4(a) and (b) interfere with each other constructively at P4 and destructively at P1. Thus, there is no reflection at P1, and the energy at the resonance frequency emerges from P4.

Although the previous two types of directional filter can realize multi-pole filtering function, there has not been an effective and general method to design multi-pole directional filter using $\lambda/2$ strip resonator structure [3.5].

Recently, an attempts to address this drawback has been reported in [3.15]-[3.16], where two identical one-pole directional filters in $\lambda/2$ -resonator form are cascaded for a two-pole filtering response. This concept is shown in Figure 3.5(a) along with its typical through- and coupled-port responses in Figure 3.5(b). The coupled port response S_{41} is similar to Butterworth filtering response with two extra transmission zeros. While this is an advancement for the directional filter structure, this method doesn't provide guidelines for realizing filtering response other than Butterworth or with higher orders. Also, there seems to be lack of control to the resulting directional filter response.

It is desirable to have a $\lambda/2$ resonator directional filter structure that can be generalized to realize N-pole response, and it would also be advantageous if we can synthesize the response of the directional filter using conventional filter synthesis technique. Numerous years of research on the filter synthesis has enabled a systematic method for designs of a great variety of filter responses, like elliptic response or response with transmission zeros at random desired

frequencies [3.6]-[3.10]. Since the hybrid-coupled directional filter is based on band-pass filter, it can harvest this systematic design method with great variety of filtering response to choose from.

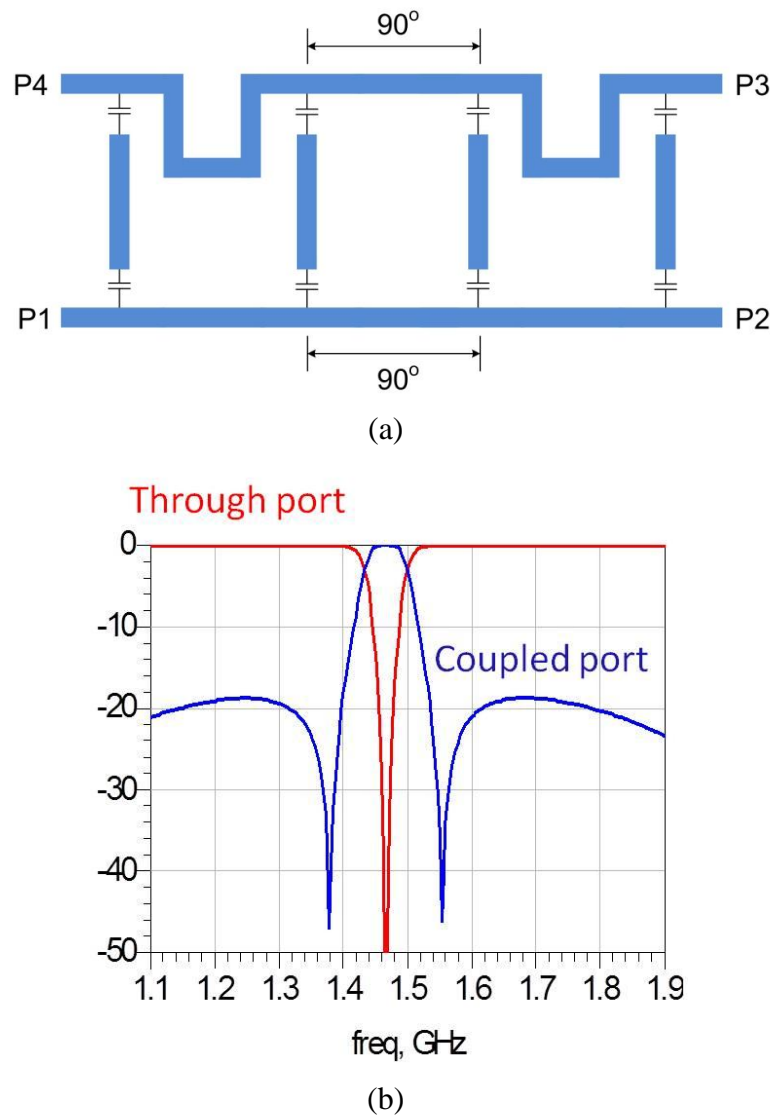


Figure 3.5 Two-stage directional filter consists of two identical single pole directional filter with 90° delay line (a), and its. typical coupled and through port responses (b).

In the remainder of the thesis, we validate, improve, and investigate the limits of a new methodology for designing $\lambda/2$ resonator directional filters based on conventional filter design. This methodology is systematic, can realize a great variety of responses other than Butterworth

and Chebyshev, and provides guidelines in realizing N-pole directional filter responses. This not only allows us to realize filtering response with higher stages, but also allows us to synthesize the directional filter response more precisely. The effectiveness of this methodology is demonstrated by prototypes with three-pole elliptical and four-pole asymmetric directional filters using $\lambda/2$ resonator structure. The success of this methodology means we can design high-performance directional filter that is easy to manufacture, which makes the directional filter more competitive with other multiplexing schemes.

3.1 BIBLIOGRAPHY

- [3.1] R.J. Cameron, and M. Yu, "Design of manifold-coupled multiplexers," IEEE Microwave Magazine, vol. 8, no. 5, pp. 46-59, 2007
- [3.2] D. S. Levinson, and R. L. Bennett, "Multiplexing with high performance directional filters," Microwave Journal, pp. 99-112, June 1989.
- [3.3] J.-S. Hong, M. J. Lancaster, R. B. Greed, D. Jedamzik, J.-C. Mage, and H. J. Chaloupka, "a high-temperature superconducting duplexer for cellular base-station applications," IEEE Tans. Microwave Theory and Techniques, vol. 48, no. 8, pp. 1336-1343, 2000.
- [3.4] S. H. Talisa, M. A. Janocko, D. L. Meier, C. Moskowitz, R. L. Grassel, and J. Talvacchio, "High-temperature superconducting four-channel filterbanks," IEEE Trans. Applied Superconductivity, vol. 5, no. 2, pp. 2079-2082, 1995.
- [3.5] G. L. Matthaei, L. Young, and E. M. T. Jones, *Microwave Filters, Impedance-Matching Networks, and Coupling Structures*. Norwood, MA: Artech House, 1980.
- [3.6] R. J. Cameron, "General coupling matrix synthesis methods for Chebyshev filtering function," IEEE Transactions on Microwave and Techniques, vol. 47, no. 4, pp. 433-441, 1999.
- [3.7] S. Amari, and M. Bekheit, "Physical interpretation and implications of similarity transformations in coupled resonator filter design," IEEE Transactions on Microwave and Techniques, vol. 55, no. 6, pp. 1139-1153, 2007.

- [3.8] J. D. Rhodes, "Waveguide bandstop elliptic function filters," *IEEE Transactions on Microwave and Techniques*, vol. 20, no. 11, pp. 715-718, 1972.
- [3.9] R. J. Cameron, M. Yu, Y. Wang, "Direct-coupled microwave filters with single and dual stopbands," *IEEE Trans. Microwave Theory & Tech*, vol. 53, no. 11, pp. 3288-3297, 2005.
- [3.10] J. -S. G. Hong, and M. J. Lancaster, "Microwave filters for RF/Microwave applications," John Wiley & Sons, 2001.
- [3.11] F. S. Coale, "a traveling-wave directional filter," *IRE Trans. Microwave Theory and Techniques*, vol. 4, no. 4, pp. 256-260, 1956.
- [3.12] J. L. B. Walker, "Exact and approximate synthesis of TEM-mode transmission-type directional filters," *IEEE Transactions on Microwave Theory and Technique*, vol. 26, no. 3, pp. 186-192, 1978.
- [3.13] S. Uysal, "Microstrip loop directional filter," *Electronics Letters*, vol. 33, no. 6, pp. 475-476, 1997.
- [3.14] Y. Cheng, W. Hong, and K. Wu, "Half mode substrate integrated waveguide (HMSIW) directional filters," *IEEE Microwave and Wireless Components Letters*, vol. 17, no. 7, pp. 504-506, 2007.
- [3.15] H. Lobato-Morales, A. Corona-Chavez, J. L. Olvera-Cervantes, D. V. B. Murthy, "Multi-pole microstrip directional filters for multiplexing applications," *International Conference on Electrical Communications and Computers*, pp. 344-349, 2011.
- [3.16] J. P. Kim, "Improved design of single-section and cascade planar directional filters," *IEEE Trans. Microwave Theory and Techniques*, vol. 59, no. 9, pp. 2206-2213, 2011.

CHAPTER 4

BRF-based Directional Filter -- Proof of Concept

Directional filter was designed a few decades ago for the purpose of multiplexing incoming signals. However, in recent years it is no longer the preferred method for multiplexing. One of the reasons is researchers gradually figured out a systematic optimization procedure to design the manifold multiplexer. However, another important reason is that the previously developed directional filter structures are either cumbersome, needs very tight manufacturing tolerance, or cannot realize multi-pole response for good filtering performance.

Starting from this chapter, we investigate and experiment a new directional filter structure that can realize good filtering performance with relaxed tolerance requirement. This allows realization of a robust high performance directional filter, putting directional filter back onto competitive ground. The new directional filter (DF) is based on band-reject filter (BRF) design, hence the name BRF-based DF.

4.1 INTRODUCTION

Here we investigate an effective method to realize multi-stage DF based on the strip-resonator type structure. Instead of cascading two DFs as shown in Figure 3.5, we cascade two identical differential band-reject filters (BRF). This concept is shown in Figure 4.1. Since the response of the BRF can be specifically designed based on the rich research in the filter

community [4.1], [4.2], this offers us an alternative way to synthesize the DF response in a more precise way.

A DF prototype is developed in this Chapter to validate this approach. The DF is based on a BRF specifically designed with an elliptic response with -22dB matching and rejection ripples and 5.5% band-width centered at 1.5GHz. It is shown that the performance of the DF can be very closely predicted by the designed BRF, thus allows us to synthesize the DF with different responses more precisely.

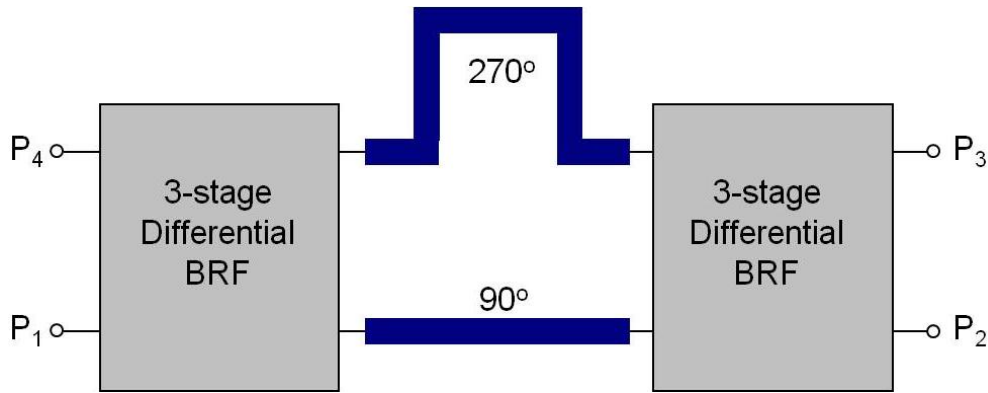


Figure 4.1 The proposed multiple-stage directional filter.

4.2 CONCEPT OF NEW DIRECTIONAL FILTER STRUCTURE

The basic one-pole strip-resonator type DF is shown in Chapter 3, and is repeated in Figure 4.2 for convenience. It consists of two identical half-wavelength resonators coupled to the two main transmission lines (TL), and the 90° and 270° delay lines connecting in between. As explained in Chapter 3, the coupled half-wavelength resonator rejects the differential excitation between the two main TLs at the resonance frequency f_o , and passes the even excitation. The function of the 90° and 270° delay lines in the middle is to switch the excitation modes between

the two main TLs after the signal passes through it. After performing the even and odd mode excitation analysis between Port 1 and Port 4, one obtains the conclusion that the S_{41} response is a single-pole band-pass response at f_0 , S_{21} is the band-reject response at f_0 complimentary to the S_{41} response, Port 3 is isolated from Port 1, and Port 1 is matched within a very wide band-width [4.3]. The detail of this analysis will be presented in Chapter 5.

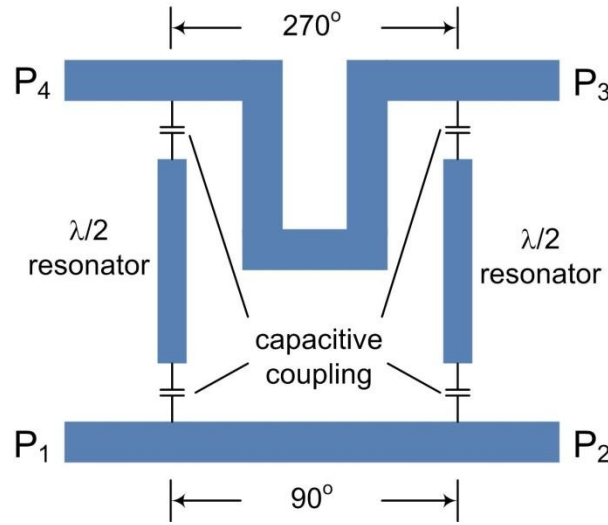


Figure 4.2 The basic one-pole $\lambda/2$ strip-resonator directional filter.

Since the half-wavelength resonator coupling into the main TL in Figure 4.2 can be thought of as an one-stage BRF that is only excited under differential excitation, our attempt to the multi-stage DF design is to augment the single half-wavelength resonator to a multi-stage differential BRF, as shown in Figure 4.1. The differential BRF used here should be designed so that it rejects differential excitation between the two main TLs, and passes the even excitation, just like the half-wavelength resonator in Figure 4.2 would. Since the underlying working mechanism of the DF just described is not disturbed, we should still obtain the directionality, but with higher-order filtering function.

In the following sections we describe the development of a three-stage elliptic function DF as the proof of concept.

4.3 BAND-REJECT FILTER FOR NEW DIRECTIONAL FILTER

The core of the development of this DF is the differential BRF. We construct this BRF based on the natural BRF prototype described in [4.1] since it allows the realization of the elliptic BRF without any complicated cross-coupling scheme.

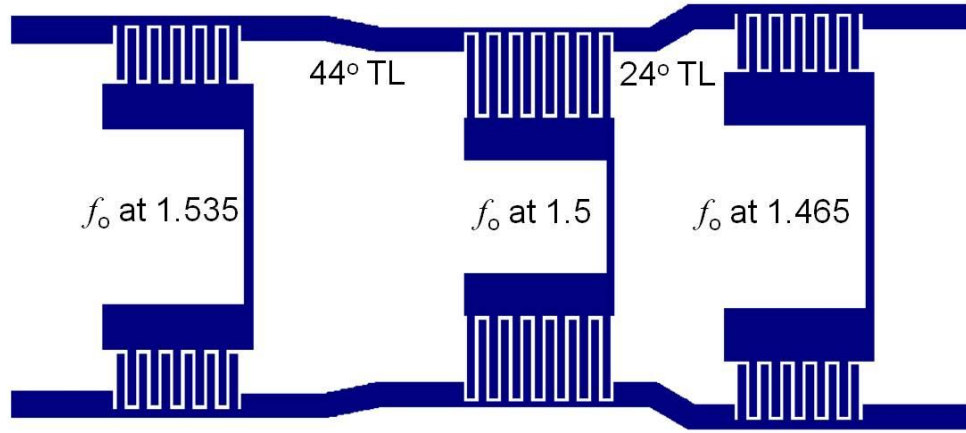


Figure 4.3 Microstrip layout for the differential BRF.

The microstrip structure for this elliptic BRF is shown in Figure 4.3. The design is based on elliptic function with -22dB ripple in both S_{11} and S_{21} with 5.5% band-width centered at 1.5GHz. We use capacitively coupled step-impedance resonators to realize the three stages. The inter-digital capacitors are made of 0.5mm wide strips and 0.3mm gaps. The three resonators resonate at 1.535GHz, 1.5GHz and 1.465GHz respectively, and the normalized impedance slope parameters (x/Z_o) of the three resonators are 13.66, 7.6, and 13.04, respectively. Ideally, the delays between the resonators should be 102° and 79° , but the size of the inter-digital capacitors

and their loading effect to the TLs must be compensated [4.3]. So the delays between the resonators are shortened to about 44° and 24° . The resonators are only excited by the odd excitation between the two main transmission lines, so the even excitation is passed to the other end.

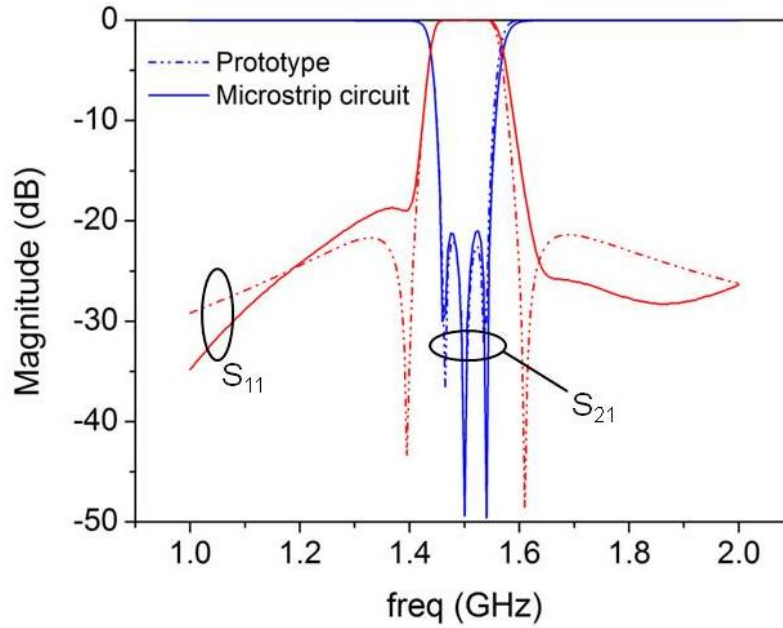


Figure 4.4 Simulated S-parameters of the BRF compared with the ideal response.

The lossless simulation response of this BRF with differential excitation is shown in Figure 4.4, along with the ideal elliptic function that it is based on. The simulated response of the microstrip structure is shown as solid lines, and the ideal elliptic response is shown as dashed lines. We can see that the S_{21} response has an equal-ripple rejection band that follows the ideal response very closely. The S_{11} response deviates from the ideal response somewhat outside the operating bandwidth. The reflection zeros in S_{11} are not as deep, and the zero position at the higher frequency range moves away from the center frequency, so the roll-off rate is not as steep. These deviations are because of the inevitable imperfection when we try to approximate the ideal

coupling matrix with real transmission lines, EM coupling structure, and resonator structures. Nevertheless, the similarity between the two responses is clearly observed.

To apply this BRF in the proposed DF, the response of the BRF under even excitation is also checked. It is an all-pass response in the frequency range of 0.5~2.5 GHz with matching level below -20dB, which satisfies the requirement to perform as a BRF in differential excitation and all-pass in even excitation.

4.4 NEW DIRECTIONAL FILTER PROTOTYPE

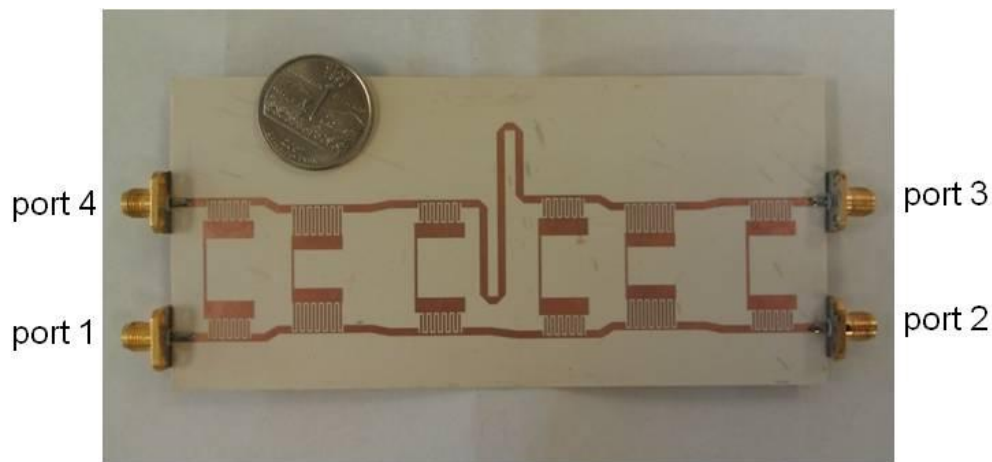
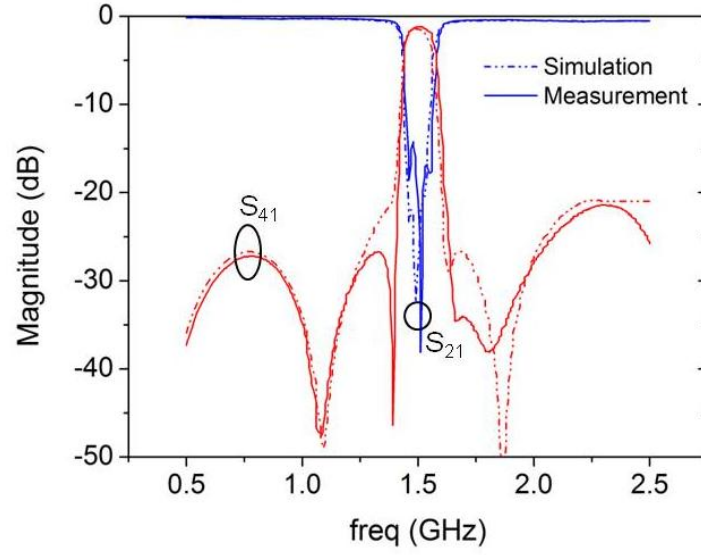
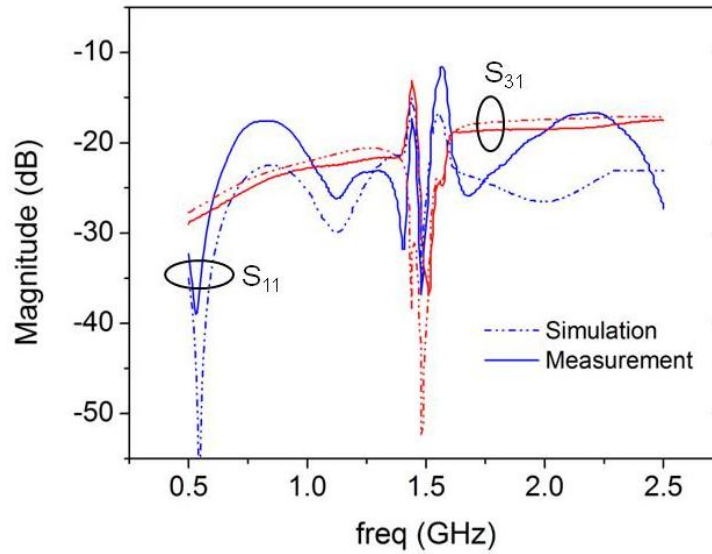


Figure 4.5 Photograph of the directional filter prototype based on the BRF in Figure 4.3.

The 3-stage elliptic function DF is built by connecting two identical BRFs introduced in Section 4.3 by delay lines, as shown in Figure 4.1. The photograph of the realized DF is shown in Figure 4.5. It is realized on Rogers RO3003 substrate with dielectric constant of 3 and thickness of 30 mil, and the size is about 14 cm long and 4.5 cm wide.



(a)



(b)

Figure 4.6 Simulated and measured S-parameter of the directional filter in Figure 4.5.

The simulated and measured responses are shown in Figure 4.6 as dashed lines and solid lines respectively. Figure 4.6(a) shows the S_{21} and S_{41} of the DF. The S_{21} response is a band-reject response centered around 1.5GHz, and there shows three rejection poles, which resembles the S_{21} response of the BRF in Figure 4.4. The signal rejected by the S_{21} response is extracted to

port 4. This is observed in the S_{41} response of the DF, which has a pass-band around 1.5GHz. Moreover, the S_{41} response resembles the S_{11} of the BRF in Figure 4.4 closely, which has elliptic function characteristics. Further, there are two additional transmission zeros generated around 1.1 and 1.9GHz in the S_{41} of the DF compared to the S_{11} of the BRF. This is due to the frequency dependence of the additional 180° phase delay in the upper main transmission line, and actually increases the rejection level in the stop-band.

Figure 4.6(b) shows the S_{11} and S_{31} response of the DF prototype. We can observe that the structure is well matched within the frequency range of 0.5~2.5GHz, and is below -12dB. Port 3 is isolated from Port 1. The S_{31} reaches -35dB at the center frequency of 1.5 GHz and levels around -17dB in the higher end of the frequency range.

4.5 CONCLUSION

In this Chapter we investigated a new methodology in designing multi-stage DF. The DF connects two differential BRF with proper delay lines. The prototype developed in this Chapter is based on the elliptic differential BRF with -22dB ripples and 5.5% band-width centered at 1.5GHz. With this prototype, we verified that the coupled-port response and through-port response of the resulting DF respectively resemble that of the S_{11} and S_{21} response of the constituting BRF. This not only allows us to synthesize the DF response in the way we desire, but also allows us to harvest the rich research resources in the conventional filter synthesis to realize higher-order or more versatile filtering response.

Now that we have proved the validity of the concept, in the following Chapters we will present the theoretical analysis of this directional filter structure to further understand its potentials and limitations.

4.6 BIBLIOGRAPHY

- [4.1] J. D. Rhodes, "Waveguide bandstop elliptic function filters," IEEE MTT-Trans., vol. 20, no. 11, pp. 715-718, Nov. 1972.
- [4.2] R. J. Cameron, M. Yu, and Y. Wang, "Direct-coupled microwave filters with single and dual stopbands," IEEE MTT Trans., vol. 53, no. 11, pp. 3288-3297, 2005.
- [4.3] J. P. Kim, "Improved design of single-section and cascaded planar directional filters," IEEE MTT-Trans., vol. 59, no. 9, pp. 2206-2213, Sep. 2011.

CHAPTER 5

Theory and Improvement of the BRF-based Directional Filter Structure

In Chapter 4, we presented the proof-of-concept of a new directional filter structure. This structure has more relaxed manufacture tolerance, and is able to realize high-performance filtering function.

In this Chapter, we will present the analysis and the theoretical performance and limitations of this new structure. Moreover, in the previous prototype, the isolation performance S_{31} was not ideal outside of the filtering bandwidth. This Chapter presents a method using Composite Right/Left Handed (CRLH) transmission line to improve the isolation performance.

5.1 INTRODUCTION

As the frequency spectrum becomes more crowded with various wireless services, high performance channel multiplexing becomes a necessity. Directional filters (DF) are promising candidates for this application, and have been the focus of a lot of research activities [5.1]-[5.12]. Compared with other types of multiplexing structures, a DF has the unique trait of wide-band matching. This permits the development of the multiplexer system to be integrated in a module by module fashion. This is particularly useful if the number of channels needed is large, where the complexity of using other types of multiplexing structures may become unmanageable [5.1].

As introduced in Chapter 3, there are three main kinds of DF, hybrid-coupled, traveling-wave loop type, and $\lambda/2$ strip-resonator type. The hybrid-coupled directional filter is cumbersome, and its usable bandwidth is limited by the 90° hybrid circuit. Although with more stages, the bandwidth of the 90° hybrid can be larger, it is hard to exceed 50% fractional bandwidth [5.5]. For the traveling-wave loop type directional filter, it is just too demanding in manufacturing tolerance.

The $\lambda/2$ strip-resonator type DF strikes a balance between the compactness and the robustness to manufacturing defects. It does not require 90° hybrid circuits, so it can be more compact than the hybrid-coupled DF. Also, its usable bandwidth can be considerably wider than the hybrid circuits. As will be demonstrated in this Chapter, an impedance bandwidth of more than 130% can be readily achieved. Compared to a traveling-wave loop type structure, it is not as compact but it does not suffer from the ultra-high sensitivity to manufacturing defects.

Realizing multi-stage DF response with this structure is the recent research focus. In [5.10]-[5.12], the idea of cascading two identical one-pole DFs for a two-stage Butterworth response is experimented and theoretically analyzed. Upon the foundation of these studies, an alternative structure has been proposed in Chapter 4. In this new band-reject filter (BRF) based structure, two identical BRFs are cascaded to form a DF. A three-pole elliptic DF prototype is also presented in Chapter 4, demonstrating the extension of the DF response to more than two-stage and response other than Butterworth or Chebyshev. However, in Chapter 4 we have not provided theoretical analysis of the structure, nor the detailed analysis of the DF performance. Also, there is certainly room for improvement for the BRF realization, since the deviation of the BRF response realized in the Chapter 4 from the ideal elliptic response is noticeable. It is

important to identify the cause of this deviation, so that when we are designing the BRF for the directional filter, we can take these factors into account.

In this Chapter, a complete theoretical analysis of this BRF-based structure is presented and different aspects of the DF performance are examined. We confirm that there exists a theoretical bound for the rejection level in the filtering response of the DF, and it completely depends on the design of the BRF. Also, there are extra transmission zeros additional to the ones in the BRF response, of which the location can be predicted using the theory presented in this Chapter. These characteristics are validated experimentally by a three-pole elliptic prototype using a new BRF modified from the one in Chapter 4. This new BRF demonstrates a good elliptic response. Excellent correspondence among DF performance, BRF performance and the theory is confirmed.

In addition to the theoretical study, an improved version of this DF structure is proposed. One potential problem of this BRF-based structure is its isolation level at frequencies other than the center frequency. As can be seen in Figure 4.6, this isolation level is around 18dB. We identify the cause of this low level of isolation, and rectify the problem utilizing Composite Right/Left Handed (CRLH) transmission lines (TL). A new DF prototype using this CRLH technique with the same BRF is fabricated to show the effectiveness of this novel idea. With this prototype incorporating CRLH TL, a wide-band isolation level of 30dB in the intended frequency range can be achieved.

5.2 THEORY OF BRF-BASED DIRECTIONAL FILTER

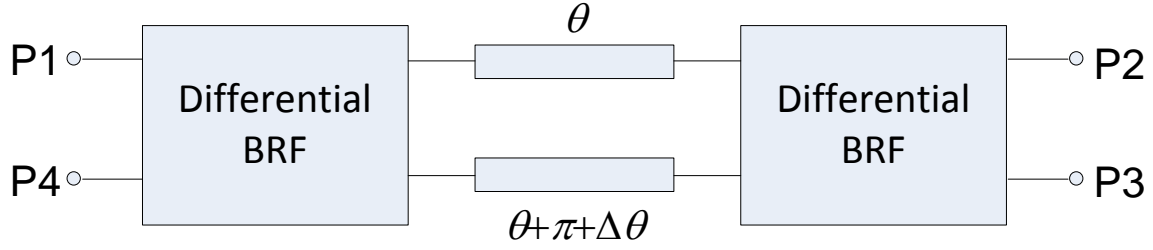


Figure 5.1 The basic structure of the BRF-based directional filter.

The basic structure for this BRF-based DF is shown in Figure 5.1. The differential BRF block is a filtering structure that behaves as a BRF when the upper and lower ports (P1 and P4 in Figure 5.1) are excited differentially, and as an all-pass filter when excited evenly. At the center frequency, ideally the delay between the two differential BRFs will have 180° phase difference, so that they switch the excitation mode from common to differential, and vice versa. Here $\Delta\theta$ represents the deviation of the phase difference of the two lines from 180° due to the frequency dependence of their phase responses. The working mechanism of this DF structure is illustrated below.

In Figure 5.2 we illustrate the situation when the signal frequency is within the rejection bandwidth of the differential BRF. When ports P1 and P4 are excited evenly, the signal will pass through the first differential BRF block since it behaves like an all-pass filter under common excitation. However, the delay lines between the two blocks have 180° phase difference around the center frequency, so the signal becomes differential when it reaches the second differential BRF, and it is reflected back to P1 and P4. When P1 and P4 are under differential excitation, the signal is reflected back to the two ports by the first differential BRF. Under normal working circumstances where only P1 is excited, the common and differential-modes are excited equally, and the two signals reflected back to P1 and P4 will interfere with each other. Thus, we can

choose θ so that the signals interfere constructively at P4 and destructively at P1. In this way, there would be no input reflection, and the signal in this frequency band is directed to P4.

The previous phenomenon occurs when the signal frequency is within the BRF rejection bandwidth. If the signal frequency is outside of the BRF bandwidth, it can pass through the differential BRF, hence reaching P2 and P3 regardless of the mode of excitation. If the two modes are excited equally, then they will interfere constructively at P2 and destructively at P3. Thus, when the signal is out of the BRF bandwidth, it goes directly from P1 to P2 and flows into the next stage.

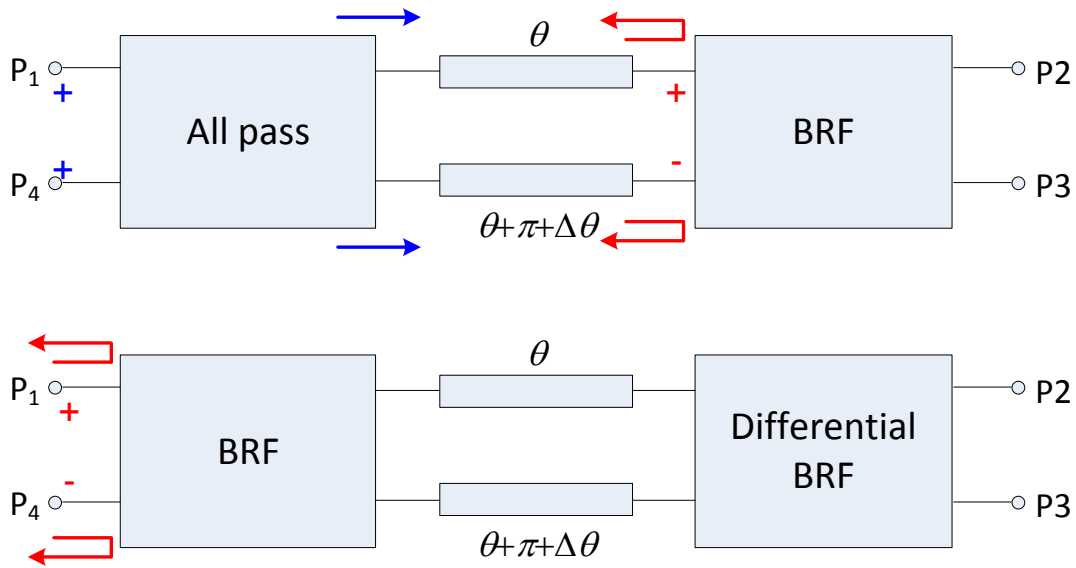


Figure 5.2 The DF structure under common and differential excitations when the signal frequency is within the rejection bandwidth of the differential BRF.

By using the S-parameters of the differential BRF block to trace the common and differential signal flows in the structure, S-parameters of the final DF can be related to the S-parameter of the differential BRF by tracing the common and differential signal flows obtained from the S-parameters of the differential BRF block, as shown in (5.1)-(5.4).

$$S_{11} = \frac{1}{2} S_{11o} \left\{ 1 + e^{-j(2\theta + \Delta\theta)} \left[S_{21e} \cos \frac{\Delta\theta}{2} + j S_{21o} \sin \frac{\Delta\theta}{2} \right]^2 \right\} \quad (5.1)$$

$$S_{21} = \frac{1}{4} (e^{-j\theta} - e^{-j(\theta + \Delta\theta)}) (S_{21o} - S_{21e})^2 + e^{-j\theta} S_{21o} S_{21e} \quad (5.2)$$

$$S_{31} = \frac{1}{2} (S_{21e}^2 - S_{21o}^2) e^{-j(\theta + 0.5\Delta\theta)} j \sin \frac{\Delta\theta}{2} \quad (5.3)$$

$$S_{41} = -\frac{1}{2} S_{11o} \{ 1 - e^{-j(2\theta + \Delta\theta)} [S_{21o}^2 \sin^2 \frac{\Delta\theta}{2} + S_{21e}^2 \cos^2 \frac{\Delta\theta}{2}] \} \quad (5.4)$$

In the equations above, S_{ij} is the S-parameter of the final DF, where $i, j=1$ to 4. The S_{ije} and S_{ijo} are the S-parameters of the differential BRF under common and differential excitation, respectively. For simplicity we assume that $S_{11e} = 0$, since the structure is of all-pass nature under common-mode excitation. We can see that $\Delta\theta$ also affects the DF performance, since when it is not zero the mode switch is not perfect. During this derivation, the multiple reflections between the two differential BRFs are neglected since they have little contribution compare to other terms.

From these equations, we can see that the DF function can be achieved by proper selection of the delay θ . Around the center frequency, we would want to design $\Delta\theta$ to be zero so that the mode switch is 100%. Under this condition, the $\sin\Delta\theta$ terms will be zero and the $\cos\Delta\theta$ terms will be one. Thus if we select $2(\arg S_{21e} + \theta)$ to be an odd multiple of π , S_{11} would be zero and S_{41} would equal to the S_{11o} of the differential BRF, where $\arg S_{21e}$ represent the angle of S_{21e} . This accomplishes the DF functionality and assures that the filtering response of the final DF will resemble the S_{11o} response of the differential BRF.

From (5.4) we can also see that there are two sources for the transmission zeros in S_{41} response. The first one is the “BRF transmission zeros” which comes from the S_{110} response that we designed for the BRF. The second one is the “extra transmission zeros” which is caused by the frequency dependency of the transmission line phase, and these extra transmission zeros are in addition to BRF transmission zeros. To see why there is extra transmission zeros, consider when frequency is not far from center frequency and $\Delta\theta$ is small. S_{41} will be zero at frequencies where $2(\arg S_{21e} + \theta + \Delta\theta)$ is an even multiple of π . This can also give a quick estimation of the extra transmission zero frequencies around the center frequency.

The major advantage of this DF structure is that the S_{41} response is bounded by S_{110} . This can be observed from (5.4), where the S_{41} response of the DF is S_{110} of the differential BRF multiplied by terms of which amplitude is bounded by one. This implies that when designing the DF to meet certain specifications, considering the design of the differential BRF to meet the specification would be a good start. This reduces the DF synthesis to conventional filter synthesis, where a lot of research and experiences have been accumulated. Also, as mentioned before, extra transmission zeros are introduced at predictable positions. This property can be included into the consideration of choosing the filter response type and number of stages for the differential BRF, which normally results in fewer stages for the same rejection requirement.

5.3 DESIGN OF DIFFERENTIAL BRF FOR ELLIPTICAL DIRECTIONAL FILTER

To validate the aforementioned theory, we develop a BRF-based DF prototype with three-pole elliptic response. As mentioned in the Section 5.2, the key to the elliptic DF is to design a differential BRF with the same elliptic response. This differential BRF design with

center frequency of 1.5GHz is shown in Figure 5.3. This differential BRF is modified and improved from the similar circuit presented in [5.13].

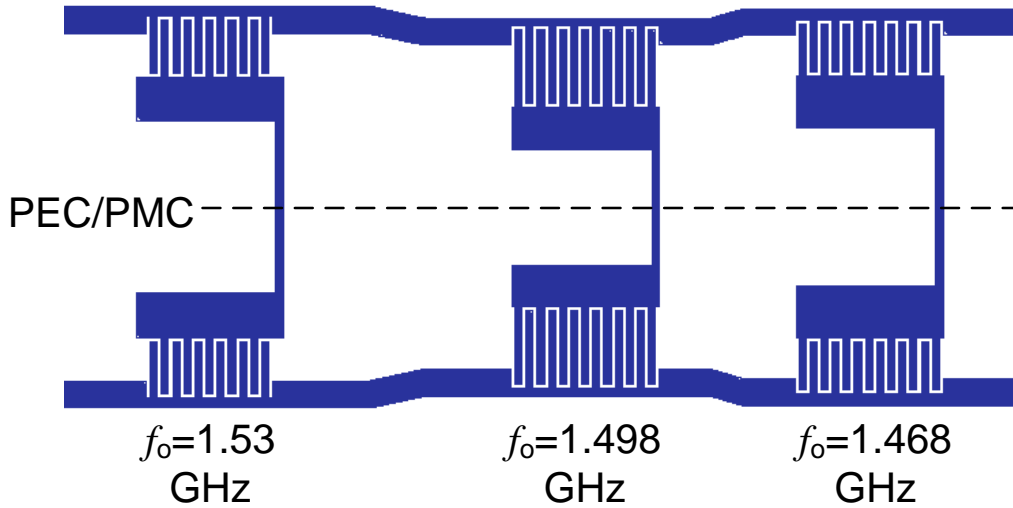


Figure 5.3 The elliptic differential BRF that the directional filter prototype is going to be based on.

When the structure in Figure 5.3 is under differential excitation, the symmetrical plane becomes a PEC plane. The resonators would present a short circuit at their resonant frequencies, and the circuit behaves as a BRF. The prototype of this BRF, including the resonance frequency of the resonators, strength of coupling to the main TL, and the phase of each TL segments, are derived analytically by following [5.17]. To realize the elliptical function, the phases of the two line segments are unequal, and are 103° and 79° respectively. However, these phases are supposed to be frequency independent in theory. To compensate for the frequency variation of the phase in reality, a Gradient optimization is run in ADS to fine tune the BRF prototype. The final result is the resonance frequencies shown in Figure 5.3 and the TL phases of 99° and 80° , respectively.

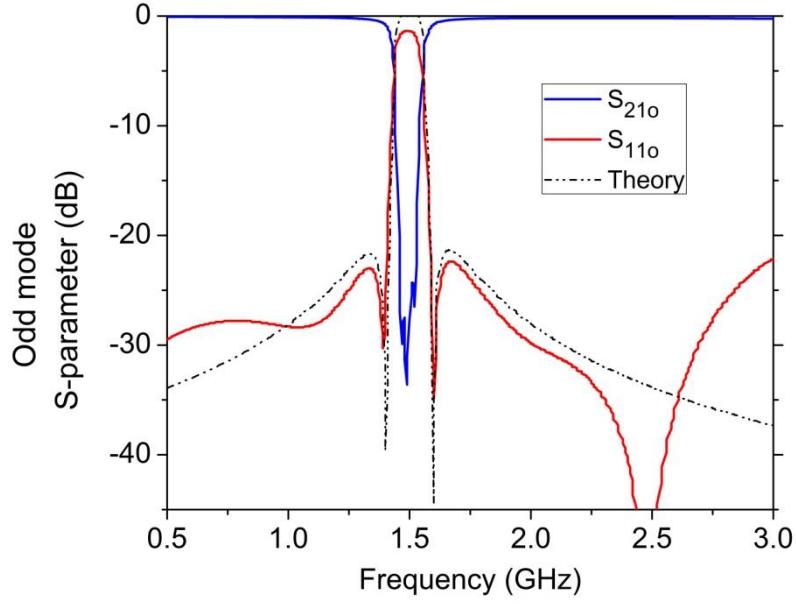
To compensate the frequency dependency of the delay lines, we need to slightly increase the characteristic impedance as well. The difference between the prototype here and in Chapter 4 is we use 52Ohm delay lines here while it was ~54Ohm for the previous prototype. This results in better even-mode matching for the BRF, and makes the realization closer to the ideal situation.

The final EM structure shown in Figure 5.3 is arrived by tuning (under differential excitation) the length of the resonators and interdigital capacitors to match the resonance frequencies and coupling strength after the Gradient optimization.

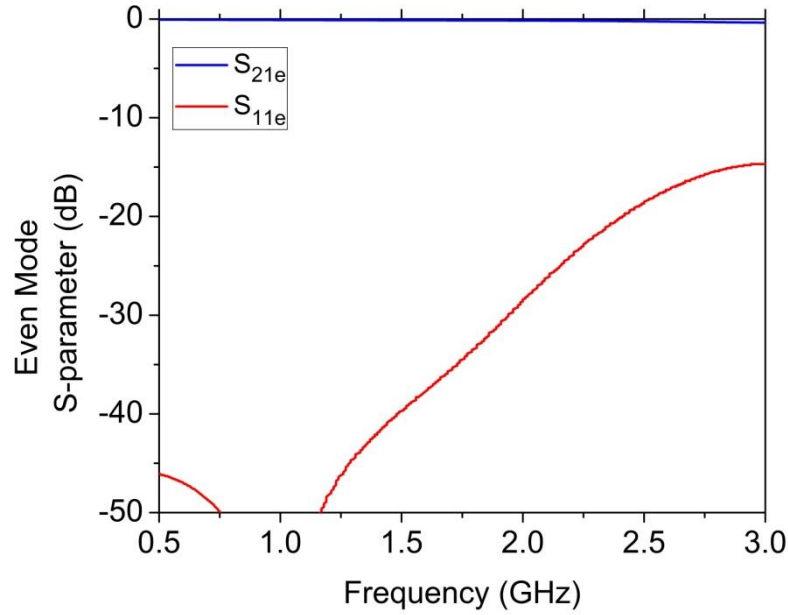
When the structure is under common-mode excitation, the symmetric plane becomes a PMC plane. The circuit then behaves as a low-pass filter due to the loading presented to the main TL by the interdigital capacitances and the open-ended stubs. Although it is not an all-pass filter as discussed in the Section 5.2, the cut-off frequency of this low-pass filter is much higher than 1.5GHz, as will be shown later.

This differential BRF is simulated by Sonnet EM, and the differential and common mode responses are shown in Figure 5.4(a) and (b), respectively. The circuit is simulated with Rogers RO3003 substrate with $\epsilon_r = 3$ and thickness of 30 mil. The simulation included material and radiation losses.

We can see that under differential excitation, it is a BRF centered at 1.5GHz with 5.5% fractional bandwidth (FBW). Furthermore, there are reflection zeros in S_{11o} response situated at around 1.4 and 1.6GHz, exhibiting the elliptic response with side-lobe level about -22dB. According to the theory presented in (5.4), the S_{41} of the final DF should also present these BRF transmission zeros at 1.4 and 1.6GHz and side-lobe level lower than -22dB.



(a)



(b)

Figure 5.4 The response of the differential BRF in Figure 5.3 under differential (a) and common-mode (b) excitations.

The theoretical elliptic response is also overlaid for comparison. The correlation between the theoretical and EM simulated response is obvious around the center frequency. The rejection

level deviates from the theoretical response below 1GHz and above 2GHz because we use real transmission lines to approximate the frequency independent phase shifts that are needed in theoretical filter prototype [5.17]. Notice the reflection zero at 2.5GHz in the simulated response. It is caused by the anti-resonances of the resonators. That is, each branch behaves like an open circuit at this frequency, hence the loading to the main transmission line is minimal.

From Figure 5.4(b) we can observe that, when under common-mode excitation, the cut-off frequency of the low-pass structure is higher than 3GHz. Thus it should not interfere with the operation of the DF.

5.4 THREE-POLE ELLIPTIC DIRECTIONAL FILTER PROTOTYPE

As mentioned in the Section 5.2, to construct the DF we need to select θ such that $2(\arg S_{21e} + \theta)$ is an odd multiple of π . From the simulation for this differential BRF, we found that $\arg S_{21e}$ is about 244° at 1.5GHz. Thus the ideal θ for DF construction is estimated to be 26° .

With this information we can also estimate the position of the extra transmission zeros in S_{41} response. As mentioned before, these extra transmission zeros occur at frequencies where $2(\arg S_{21e} + \theta + \Delta\theta)$ is an even multiple of π . Around 1.5GHz we can approximate the frequency variation of $\arg S_{21e} + \theta$ to be $(244^\circ + 26^\circ)f/f_o$ using dispersionless transmission line model, and the frequency variation of $\Delta\theta$ to be $(180^\circ)f/f_o$. Thus, the pair of extra transmission zeros closest to the center frequency can be estimated to be at 1.2GHz and 1.8GHz.

This DF uses Rogers RO3003 substrate with $\epsilon_r = 3$ and thickness of 30 mil, and the fabricated prototype is shown in Figure 5.5. The actual length of θ is found to be 27° by EM simulation with Sonnet EM, which is very close to the theoretical prediction. Simulated and

measured performances of this DF are shown in Figure 5.6. The measurements are shown in solid lines, and simulations are shown in dotted lines.

We can see the measurement corresponds to the simulation very well, except for a small frequency shift of about 1.3%. The insertion loss is about 1.2dB for S_{41} , and 0.4~0.7dB for S_{21} , and the FBW of S_{41} is about 5%. The BRF transmission zeros in S_{41} are recorded at 1.42GHz and 1.62GHz in Figure 5.6(a), which correlate very well with the response of the differential BRF and confirm the earlier theoretical analysis of (5.4). Also, the extra transmission zeros in S_{41} are also observed. The pair of extra transmission zeros that are closest to the center frequency are located at 1.1GHz and 1.9GHz, which are close to the earlier prediction with deviation less than 8.5%. The deviation mainly comes from the assumption of $\sin\Delta\theta = 0$ and $\cos\Delta\theta=1$. The frequencies of this transmission zero pair is about 27% away from the center frequency, and this assumption is not entirely true. However, it still serves as a good estimation of the positions of this transmission zero pair. If accurate prediction for transmission zero frequencies is desired, then the full formula for S_{41} in (5.4) should be used.

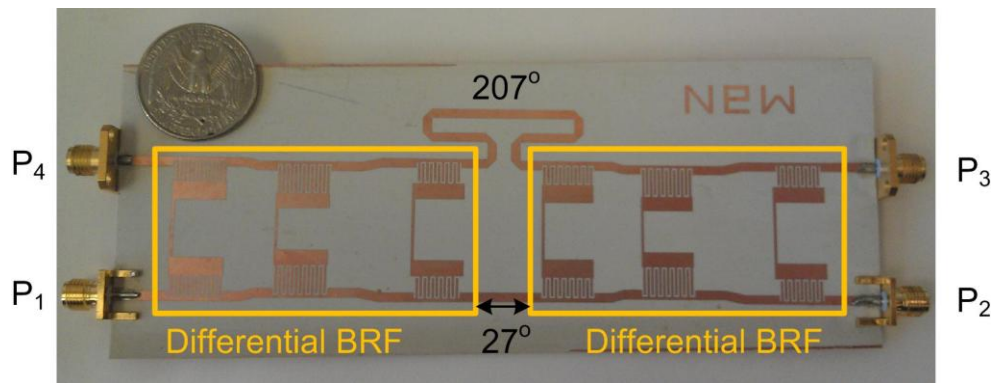
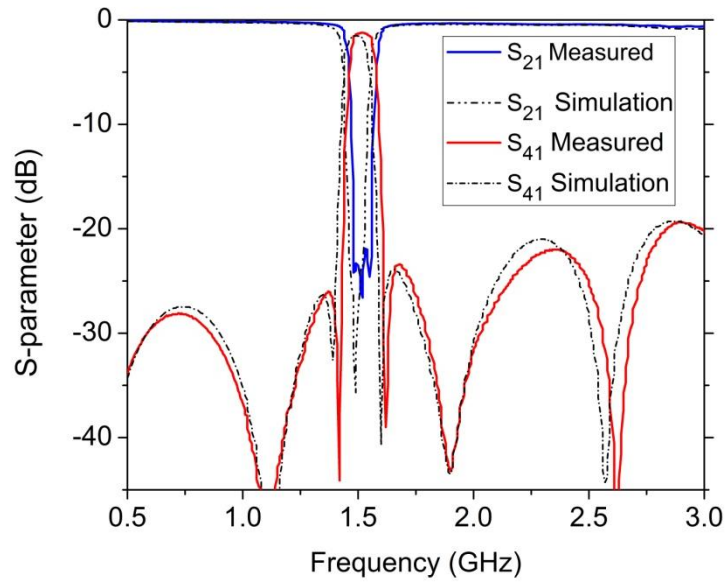
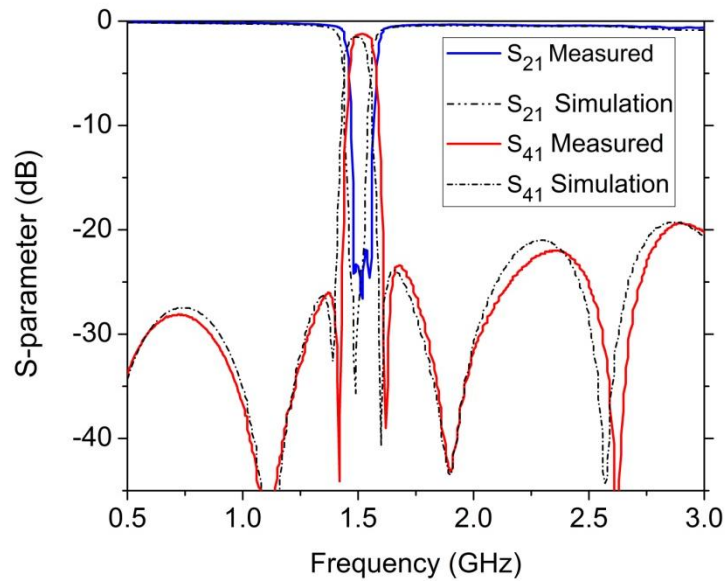


Figure 5.5 The photo of the constructed BRF-based Directional Filter using the differential BRF in Figure 5.3.



(a)



(b)

Figure 5.6 The measured S-parameters of the three-pole elliptic directional filter prototype.

Figure 5.6(b) shows the S_{11} and S_{31} response of the DF. We can see that within a bandwidth of 130%, the structure has S_{11} lower than -17dB and isolation between ports P3 and P1 better than 18dB.

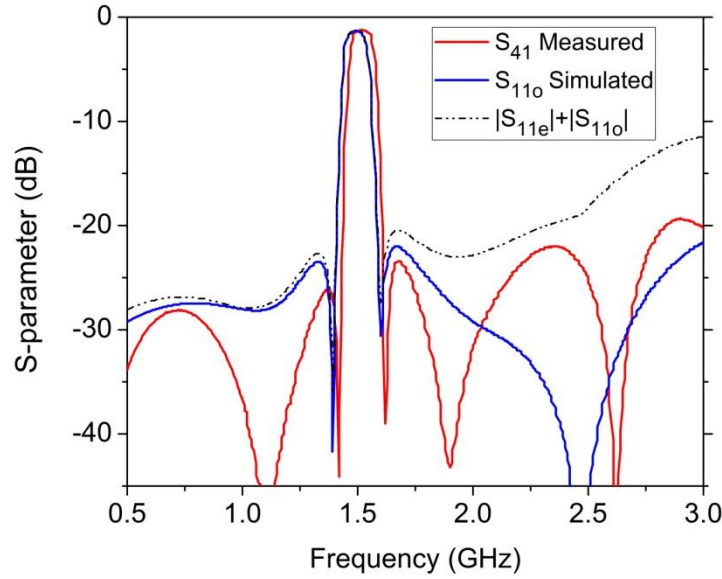


Figure 5.7 The S_{41} filtering response of the DF overlaid with S_{11o} of the differential BRF and the modified bound for S_{41} in practice.

Lastly, it is important to examine how well the S_{41} will be bounded by S_{11o} of the differential BRF in practice as claimed previously. Figure 5.7 shows the measured S_{41} response of the DF overlaid with the simulated S_{11o} of the differential BRF in Figure 5.4(a). We can see that at lower frequency side from center frequency, the S_{41} is truly bounded by S_{11o} of the BRF. However, at higher frequency ranges the S_{41} has ripple levels that exceed S_{11o} at some frequencies. This is because when deriving (5.1)-(5.4), S_{11e} of the differential BRF is assumed to be zero. By observing the S_{11e} of the realized differential BRF in Figure 5.4(b), we can see at frequencies higher than 2GHz the level of S_{11e} exceeds the rejection level of S_{11o} , and becomes the dominant factor. By going through similar theoretical derivation but including the effect of

S_{11e} , one can show that in practice the absolute bound of S_{41} should be as shown in (5.5). This modified bound is also overlaid in Figure 5.7. One thing to note is that this bound over-estimates the effect that S_{11e} might actually have, so it represents the absolute worst case.

$$|S_{41}| < (|S_{11o}| + |S_{11e}|) \quad (5.5)$$

This observation shows that the rejection level of S_{41} filtering function is also affected by the S_{11e} of the differential BRF. So in a system where particular high rejection is needed, one must also pay close attention to the level of S_{11e} . However, because of the additional transmission zero pair, the rejection level of S_{41} will generally be better than S_{11o} up to the frequency of the first additional transmission zero. In this prototype, it is shown that the S_{41} filtering response has better rejection level than S_{11o} up to $1.35f_0$.

5.5 ISOLATION IMPROVEMENT USING CRLH TRANSMISSION LINE

When observing the performance of the DF prototype in Figure 5.6, one can notice that the isolation between P1 and P3 is very good around the center frequency, but degrades pretty rapidly at other frequencies. Figure 5.6 shows isolation levels around 18dB at higher frequencies. This may not be a problem if all the channels in the multiplexing system are receiving channels, but might be problematic if some channels are transmitting high power using a common antenna with the receiving channels.

This situation is shown in Figure 5.8, where the received signal is interfered by a poorly isolated strong transmitting signal. Thus in this section we present a method to increase the isolation level to alleviate this problem while keeping other desirable advantages.

By observing the formulation of S_{31} in (5.3), we note that the isolation level is directly proportional to $\sin\Delta\theta/2$. Although we design the $\Delta\theta$ to be zero at the center frequency, it increases as we move away from the center frequency because of the difference in the phase slope of the two microstrip delay lines. Thus the isolation performance is very good at the center frequency where $\Delta\theta$ is zero, but becomes poorer away from the center frequency.

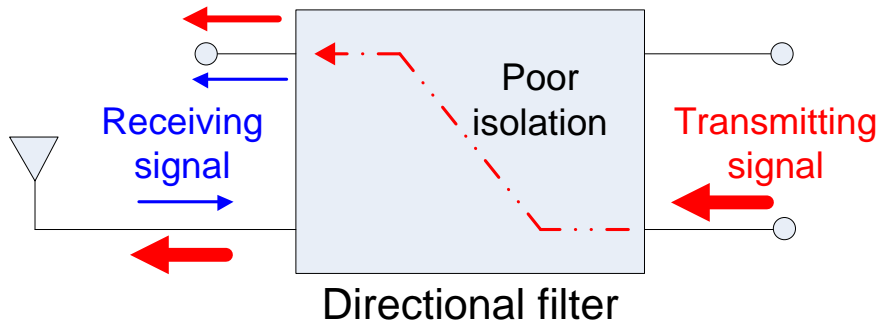


Figure 5.8 The potential problem of a directional filter if isolation is poor.

Composite Right/Left Handed (CRLH) TL have been studied extensively due to their ability to have their phase engineered [5.19]-[5.21]. For conventional TL, the passband starts at DC and the phase starts to increase with frequency from zero. Furthermore, the rate of change of the phase v.s. frequency is proportional to the phase shift. Hence, for a short section of conventional TL, the phase shift is small and the phase slope is also small. And for a long section of TL line, both phase shift and phase slope are large. However, the CRLH TL is a high-pass structure whose passband starts at a non-zero frequency. The main advantage of CRLH TL in microwave engineering is that at the start of the pass-band, both the phase shift and the phase

slope are large, and this start frequency of the pass-band can be designed. Thus, by proper designing of CRLH TL, its phase slope can match that of a long microstrip line at a certain frequency, and maintain a relative constant phase difference with this microstrip line over a

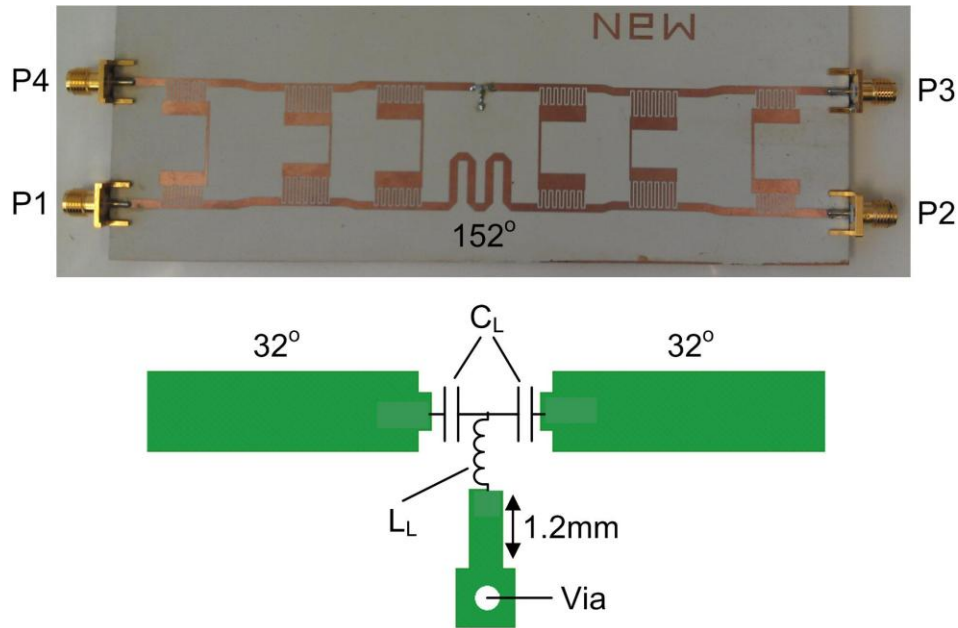


Figure 5.9 The photograph of the Directional Filter incorporating CRLH phase matching, and the realization of CRLH transmission line.

reasonable frequency range [5.21]. Here we adopt this concept to match the phase slope of the two different delay lines in the DF structure, so that $\Delta\theta$ is maintained small over a wider frequency range. However, here we face a restriction that θ is a predetermined delay for directionality performance; where in [5.21] it is a design freedom.

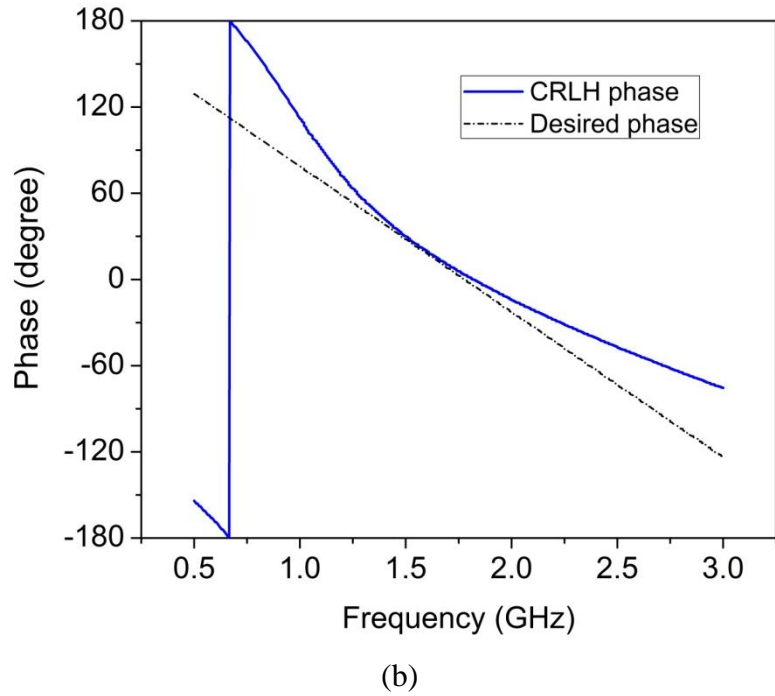
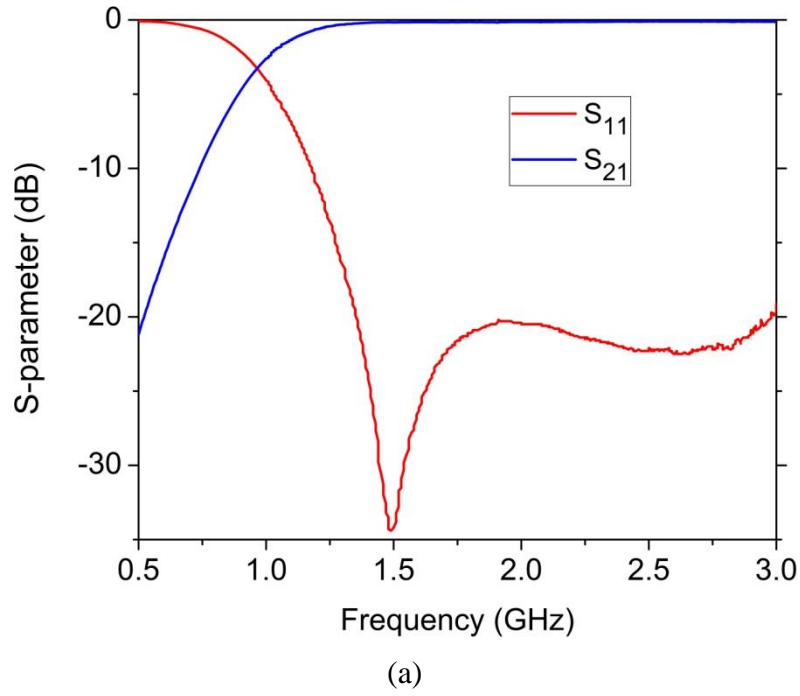


Figure 5.10 The S-parameter (a) and the phase response (b) of the CRLH transmission.

The DF prototype incorporating the CRLH phase matching scheme is shown in Figure 5.9. It uses the same differential BRF shown in Figure 5.3. Note that since the phase of CRLH

TL has to match to a long microstrip line, $\theta = 27^\circ$ in the original design is too short to work with the CRLH line, and the differential BRF at the right is flipped to resolve this problem. Since the simulated S_{11o} and S_{22o} of the differential BRF has the same amplitude but 247° phase difference at center frequency, theoretically θ should be chosen as 150° at 1.5GHz instead of 27° . In EM simulation, we found this delay to be 152° as shown in Figure 5.9, which is very close to the theoretical value. This 152° delay is realized by the microstrip line. Thus the other delay line will be designed as a CRLH transmission line with 28° phase advance at 1.5GHz and the same phase slope as a 152° microstrip line.

The realization of the CRLH line part of this DF is also shown in Figure 5.9. A single unit cell of the left-hand transmission line is in the middle of the structure. The series capacitor C_L is realized by a surface mount capacitor of 2.2pF, and the shunt inductance is realized by a surface mount inductor L_L of 4.7nH plus a short section of shorted stub. The right-hand part is realized by $50\ \Omega$ microstrip lines with 32° delay. The structure is designed so that we obtain the best matching condition at the center frequency of 1.5GHz with the desired phase delay and phase slope.

The simulated performance of this CRLH line is shown in Figure 5.10, where the amplitude of its S-parameter is shown in Figure 5.10(a) and the phase response of its S_{21} in Figure 5.10(b). The desired phase response to match that of the microstrip line is also shown in Figure 5.10(b) for comparison. We can see that the structure is of high-pass nature with cut-off frequency around 1.25GHz, and has a zero in S_{11} around 1.5GHz. The phase of the structure is 30° at 1.5GHz, and follows the desired phase response closely.

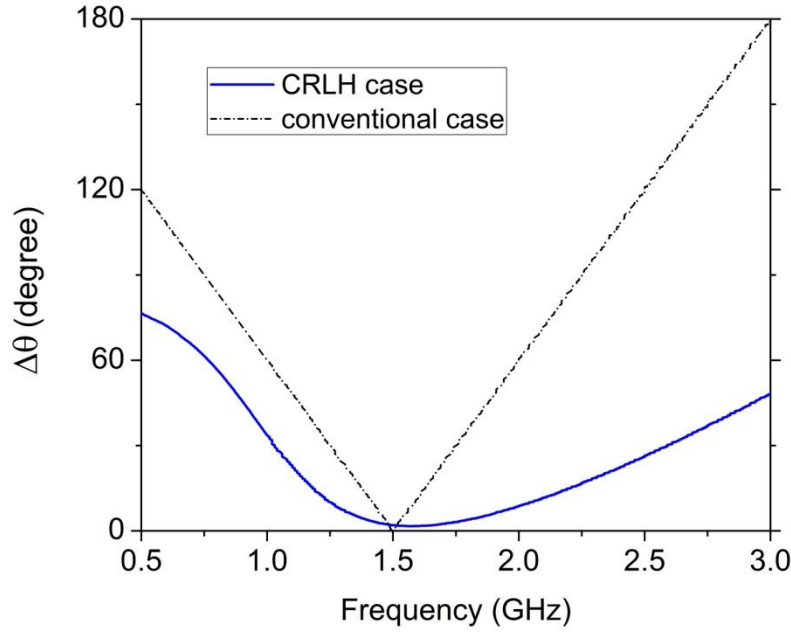
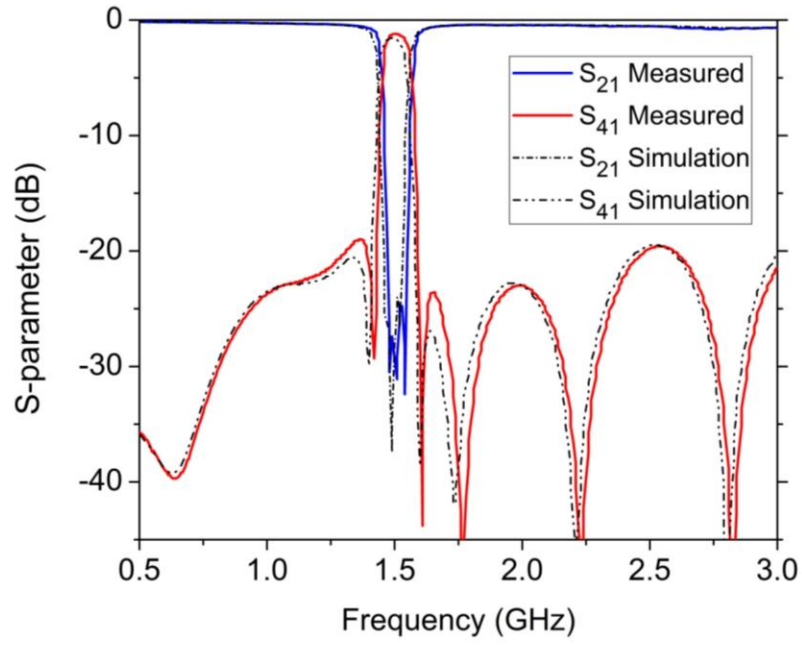


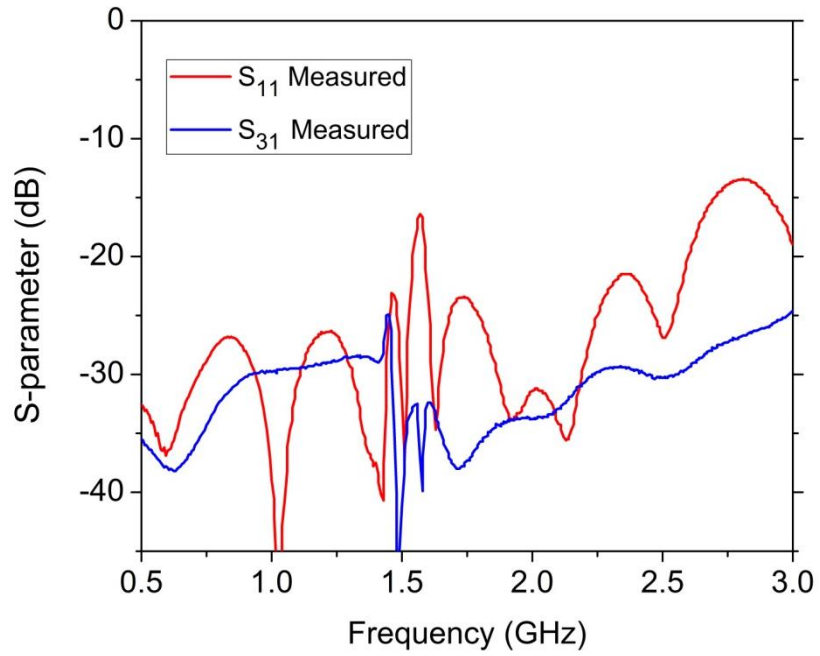
Figure 5.11 The $\Delta\theta$ comparison between the directional filter with and without the CRLH phase matching.

The improvement of using this CRLH phase matching scheme over the conventional case can be clearly seen in Figure 5.11, where the magnitude of $\Delta\theta$ is plotted for both conventional case and CRLH case. For a wide frequency range of 0.5~3GHz the CRLH case demonstrates less $\Delta\theta$ than the conventional case.

The simulated and measured performance of this DF prototype using CRLH phase matching is shown in Figure 5.12. The measured and simulated S_{21} and S_{41} response is shown in Figure 5.12(a). The measurement corresponds very well with the simulation, and the sharp elliptic filtering response is preserved. Also, the extra transmission zeros appear more frequently and are closer to the center frequency. This is because the larger θ we used in this design. Since larger θ at 1.5GHz results in larger phase slope, the period of which the additional zeros appear is reduced. The matching and isolation of this DF is shown in Figure 5.12(b).



(a)



(b)

Figure 5.12 The S-parameter response of the directional filter with CRLH phase matching, exhibiting high isolation.

Only the measured responses are shown for the clarity of the figure. The structure is well matched with S_{11} lower than -12 dB, and the isolation maintains a level around -30dB for a very wide frequency range. Compared to the isolation performance of the conventional case in Figure 5.6, it shows an improvement over 12dB.

In high-power application the insertion loss is critical. However, compared to the three-stage prototype without CRLH phase-matching, the insertion loss only increased ~0.25dB maximum across the frequency band of 0.5~3GHz.

5.6 CONCLUSION

In this Chapter, we provided a detailed analysis of the multi-stage BRF-based DF structure we proposed. The S_{41} filtering response resembles the S_{11o} response of the differential BRF it is based on. Moreover, the structure is capable of generating extra transmission zeros in S_{41} response at predictable locations, increasing the rejection level in the stop-band. The rejection level is theoretically limited by the common-mode matching S_{11e} of the differential BRF, but the three stage prototype still demonstrates low rejection level within a 70% FBW thanks to good S_{11e} and extra transmission zeros. From the multiplexer design point of view, this means that in order for the DF to meet the channel filtering requirement, it is sufficient to design the differential BRF to meet the specifications. This reduces the DF response design to the BRF design, which has been extensively researched and experimented.

One potential problem of this multi-stage DF structure is that the isolation level may not be high enough at frequencies other than the center frequency. The original prototype demonstrates an isolation level around 18dB. This can be rectified by applying CRLH phase matching for the delay lines connecting the two differential BRFs with a small penalty in

insertion loss ($\sim 0.25\text{dB}$). A wide-band isolation level of 30dB is achieved by incorporating the CRLH phase-matching in the BRF-based DF prototype.

5.7 BIBLIOGRAPHY

- [5.1] D. S. Levinson, and R. L. Bennett, "Multiplexing with high performance directional filters," *Microwave Journal*, pp. 99-112, June 1989.
- [5.2] S. B. Cohn, and F. S. Coale, "Directional channel-separation filters," *IRE Proceedings*, vol. 44, no. 8, pp. 1018-1024, 1956.
- [5.3] J.-S. Hong, M. J. Lancaster, R. B. Greed, D. Jedamzik, J.-C. Mage, and H. J. Chaloupka, "a high-temperature superconducting duplexer for cellular base-station applications," *IEEE Tans. Microwave Theory and Techniques*, vol. 48, no. 8, pp. 1336-1343, 2000.
- [5.4] S. H. Talisa, M. A. Janocko, D. L. Meier, C. Moskowitz, R. L. Grassel, and J. Talvacchio, "High-temperature superconducting four-channel filterbanks," *IEEE Trans. Applied Superconductivity*, vol. 5, no. 2, pp. 2079-2082, 1995.
- [5.5] T. K. Kataria, S.-P. Sun, A. Corona-Chavez, and T. Itoh, "New approach to hybrid multiplexer using composite right-left handed lines," *IEEE Microwave and Wireless Components Letters*, vol. 21, no. 11, pp. 580-582, 2011.
- [5.6] F. S. Coale, "a traveling-wave directional filter," *IRE Trans. Microwave Theory and Techniques*, vol. 4, no. 4, pp. 256-260, 1956.
- [5.7] J. L. B. Walker, "Exact and approximate synthesis of TEM-mode transmission-type directional filters," *IEEE Transactions on Microwave Theory and Technique*, vol. 26, no. 3, pp. 186-192, 1978.
- [5.8] S. Uysal, "Microstrip loop directional filter," *Electronics Letters*, vol. 33, no. 6, pp. 475-476, 1997.
- [5.9] Y. Cheng, W. Hong, and K. Wu, "Half mode substrate integrated waveguide (HMSIW) directional filters," *IEEE Microwave and Wireless Components Letters*, vol. 17, no. 7, pp. 504-506, 2007.

- [5.10] H. Lobato-Morales, A. Corona-Chavez, J. L. Olvera-Cervantes, D. V. B. Murthy, "Multi-pole microstrip directional filters for multiplexing applications," International Conference on Electrical Communications and Computers, pp. 344-349, 2011.
- [5.11] H. Lobato-Morales, A. Corona-Chavez, T. Itoh, and J. L. Olvera-Cervantes, "Dual-band multi-pole directional filter for microwave multiplexing applications," IEEE Microwave and Wireless Components Letters, vol. 21, no. 12, pp. 643-645, 2011
- [5.12] J. P. Kim, "Improved design of single-section and cascade planar directional filters," IEEE Trans. Microwave Theory and Techniques, vol. 59, no. 9, pp. 2206-2213, 2011.
- [5.13] J. S. Sun, H. Lobato-Morales, A. Corona-Chavez, and T. Itoh, "New approach to multi-stage directional filter based on band-reject filter design," IEEE International Microwave Symposium in Montreal, Canada, June 17-22, 2012.
- [5.14] G. L. Matthaei, L. Young, and E. M. T. Jones, *Microwave Filters, Impedance-Matching Networks, and Coupling Structures*. Norwood, MA: Artech House, 1980.
- [5.15] R. J. Cameron, "General coupling matrix synthesis methods for Chebyshev filtering function," IEEE Transactions on Microwave and Techniques, vol. 47, no. 4, pp. 433-441, 1999.
- [5.16] S. Amari, and M. Bekheit, "Physical interpretation and implications of similarity transformations in coupled resonator filter design," IEEE Transactions on Microwave and Techniques, vol. 55, no. 6, pp. 1139-1153, 2007.
- [5.17] J. D. Rhodes, "Waveguide bandstop elliptic function filters," IEEE Transactions on Microwave and Techniques, vol. 20, no. 11, pp. 715-718, 1972.
- [5.18] J. -S. G. Hong, and M. J. Lancaster, "Microwave filters for RF/Microwave applications," John Wiley & Sons, 2001.
- [5.19] C. Caloz, and T. Itoh, "Novel microwave devices and structures based on the transmission line approach of meta-materials," Microwave Symposium Digest MTT-S, pp. 195-198, 2003.
- [5.20] H. V. Nguyen, and C. Caloz, "Metamaterial-based dual-band six-port front-end for direct digital QPSK transceiver," Electrotechnical Conference MELECON, pp. 363-366, 2006.

- [5.21] C.-J. Lee, K. M. K. H. Leong, and T. Itoh, "Metamaterial transmission line based bandstop and bandpass filter designs using broadband phase cancellation," Microwave Symposium Digest MTT-S, pp. 935-938, 2006.

CHAPTER 6

Compact 4-pole BRF-based Directional Filter with Even-mode Matching Circuit for Sharp Cut-off

One of the main advantage of this BRF-based directional filter structure is that it can adapt any differential BRF and its performance. This Chapter, we demonstrate this aspect of the BRF-based DF by using another more compact differential BRF structure. By using this compact BRF structure, miniaturization of 30% is achieved with four-pole directional filter when compared with the three-pole directional filter prototype in Chapter 5.

At the same time, we increase the poles of the filtering function to four for this prototype to see if the directional filter performance can follow the BRF design for even sharper and deeper cut-off. As will be shown, when the cut-off ripple level is smaller than -30dB, the matching of the even-mode for the differential BRF has a significant effect, while it was mostly ignored in the previous studies.

6.1 INTRODUCTION

In Chapter 5, the BRF-based DF structure is studied in detail. It demonstrates prototypes with good S_{41} band-pass response with natural elliptic BRF prototype [6.1], and high isolation

performance S_{31} using composite right/left handed (CRLH) transmission line (TL) for phase-matching.

However, there seems to be a potential drawback with the DF prototypes demonstrated in Chapter 4 and Chapter 5. The resonators of the BRF have to be cascaded laterally. As the filter order becomes higher, the total structure becomes longer, which leads to large phase-shift in even-mode signal. This leads to rapid change in the phase of S_{21e} versus frequency as well. As can be seen from (5.4), which is repeated here as (6.1), The S_{41} response strongly depends on the phase of S_{21e} around center frequency where $\Delta\theta = 0$. Thus the fast change in the phase of S_{21e} will result in discrepancy between S_{41} and the BRF performance in frequencies immediately away from the center frequency.

$$S_{41} = -\frac{1}{2}S_{11o}\{1 - e^{-j(2\theta+\Delta\theta)}[S_{21o}^2 \sin^2 \frac{\Delta\theta}{2} + S_{21e}^2 \cos^2 \frac{\Delta\theta}{2}]\} \quad (6.1)$$

To deal with this problem, and for a more compact structure, we adapt the direct-coupled BRF structure [6.2] into our DF design. In this class of BRF, the resonators are cascaded in the vertical direction instead of lateral direction, which will be shown later. The advantage of this BRF structure in DF design is that the phase-shift between the two ends is maintained to be around 90° regardless of the number of the stages. Thus we can expect that, even with higher number of poles, the final DF performance will resemble that of the designed BRF for a reasonable bandwidth, similar to the three-pole DF prototype presented in previous Chapters. Also, as mentioned in the introduction to CRLH TL in Section 5.5, CRLH TL is used to match the phase a relative long conventional TL, and does not work well if the conventional TL is too

short. With the adaption of this new BRF structure, since S_{21e} is fixed to 90° regardless of the number of poles, the connecting transmission lines will always be 180° , which is convenient to work with CRLH.

As a proof of concept, a four-pole DF based on the direct-coupled BRF is demonstrated with CRLH phase-matching for improved isolation.

6.2 4-POLE BRF DESIGN

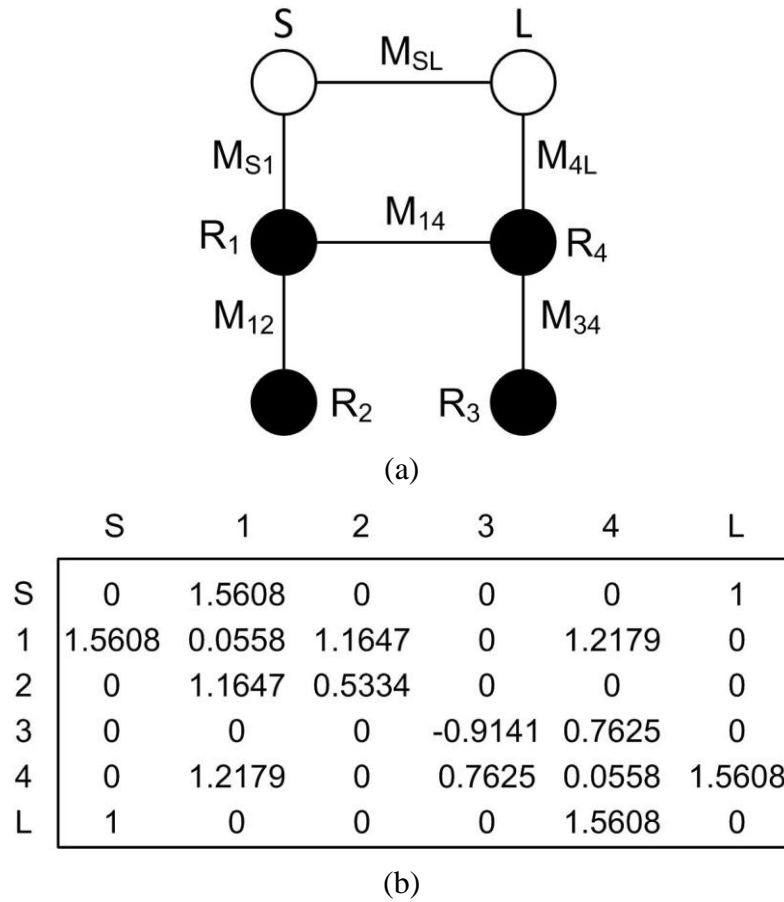


Figure 6.1 The filter structure of the BRF (a) and the corresponding coupling matrix used in this work (b).

The 4-pole direct coupled BRF structure [6.2] we are going to incorporate is shown in Figure 6.1(a), where black solid circles stand for the four resonators R_1 through R_4 , the connecting lines represents the coupling M_{ij} , and the hollowed circles represent the source and load. The corresponding coupling matrix synthesized for this demonstration is shown in Figure 6.1(b). The filter is cascaded in the vertical direction and is designed to have one reflection zeros in the higher pass-band with S_{11} of -35dB outside of stop-band and rejection of -23dB in the stop-band. The resulting S-parameter is later shown in dotted line in Figure 6.3.

The microstrip realization of this BRF is shown in Figure 6.2 The source to load coupling M_{SL} is realized by a 90° transmission line close to 50Ohm, coupling M_{1s} and M_{4L} are realized by interdigital capacitors, and the rest of the coupling is realized by proximity coupling. The resonators are $\lambda/4$ resonators, and resonator R2 and R3 is meandered to fit in the available space.

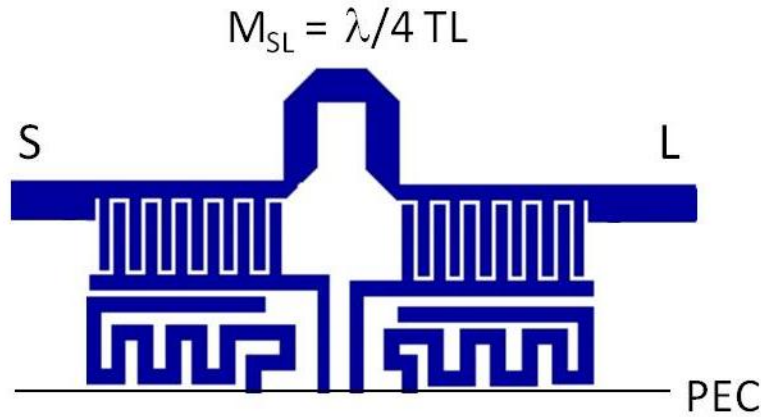


Figure 6.2 The microstrip realization of the 4-pole BRF of Figure 6.1(a).

The S-parameter of this microstrip BRF is shown in Figure 6.3 in solid line, with the ideal response from coupling matrix calculation in dotted line. The center frequency is designed to be at 1.7GHz with FBW ~5.7%. The responses are asymmetric and have a zero in S_{11} response

at 1.8GHz. In the realized response, the lower two zeros in S_{21} merged together, the rejection level is about 20dB in the stop-band, and the cut-off rate is somewhat slower at frequencies away from the center frequency. These are caused by deviations of the real microwave circuits from the ideal elements used in the coupling matrix synthesis. However, the S_{11} response still resembles the ideal ones, and preserves the zeros and the sharp cut-off behavior.

The source to load coupling M_{sL} in the ideal coupling matrix is 1, which should translate to 50 Ohm quarter wave transmission line in microstrip circuit. However, in the actual realized circuit in Figure 6.2 it is 55 Ohm instead. This is because the phase response of this quarter-wave transmission line is frequency dependent. In order to compensate for this effect, some increase in the characteristic impedance of the line and slight tuning in the resonators are necessary.

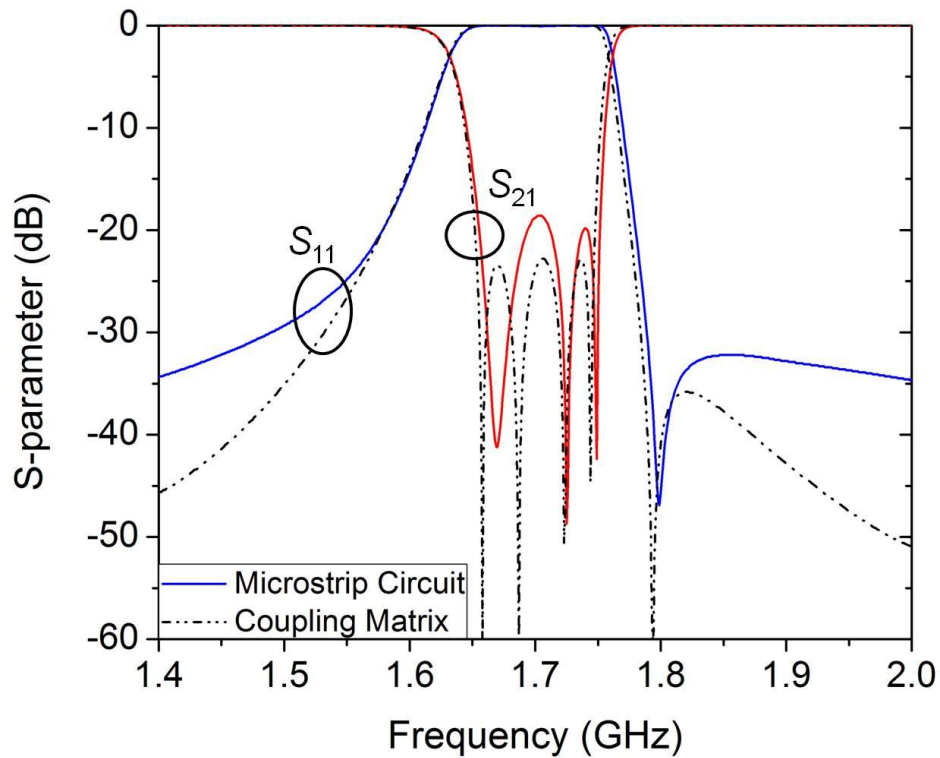


Figure 6.3 BRF response from the coupling matrix (dotted) and the microstrip circuit (solid).

6.3 4-POLE DIRECTIONAL FILTER PROTOTYPE

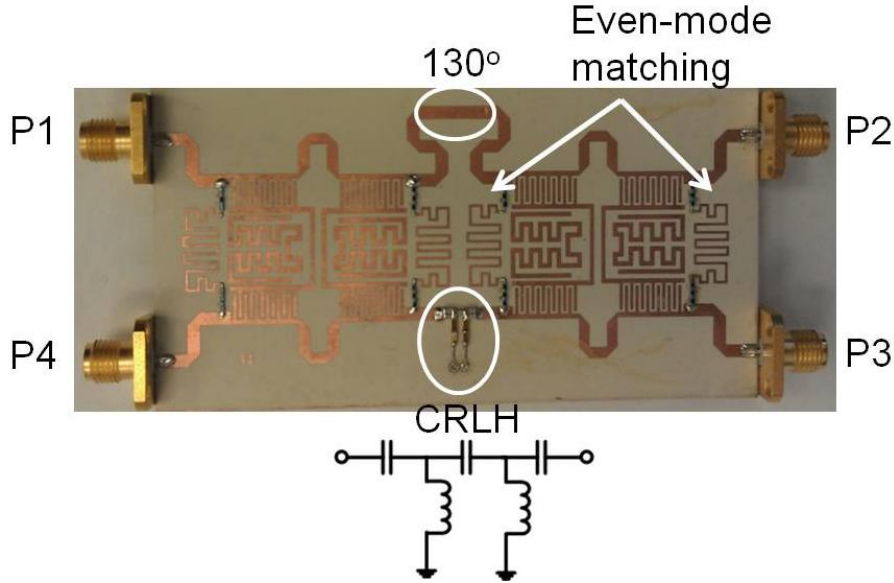


Figure 6.4 The realized DF prototype using the 4-pole BRF in Figure 6.2.

To use this BRF for a DF design, we first mirror the structure in Figure 6.2 with respect to the PEC plane. In this way it will preserve the BRF performance under odd-mode excitation, but will be an all-pass filter under even-mode excitation. This condition is necessary to construct a DF using the BRF. The proper delay line between the two mirrored BRFs is found to be 130° . Notice this delay line is larger than 90° , and according to Chapter 5, this is ideal to work with CRLH phase-matching. This is due to the fixed phase-shift ($\sim 90^\circ$) in the direct-coupled BRF structure regardless of the order of the filter.

The fabricated prototype is shown in Figure 6.4. We can see that the two mirrored BRFs are connected by 130° microstrip line and the CRLH TL. It is fabricated on RO3003 substrate with $\epsilon_r=3$ and thickness of 30mil. The size of the DF is about 89mm x 32mm. The CRLH line

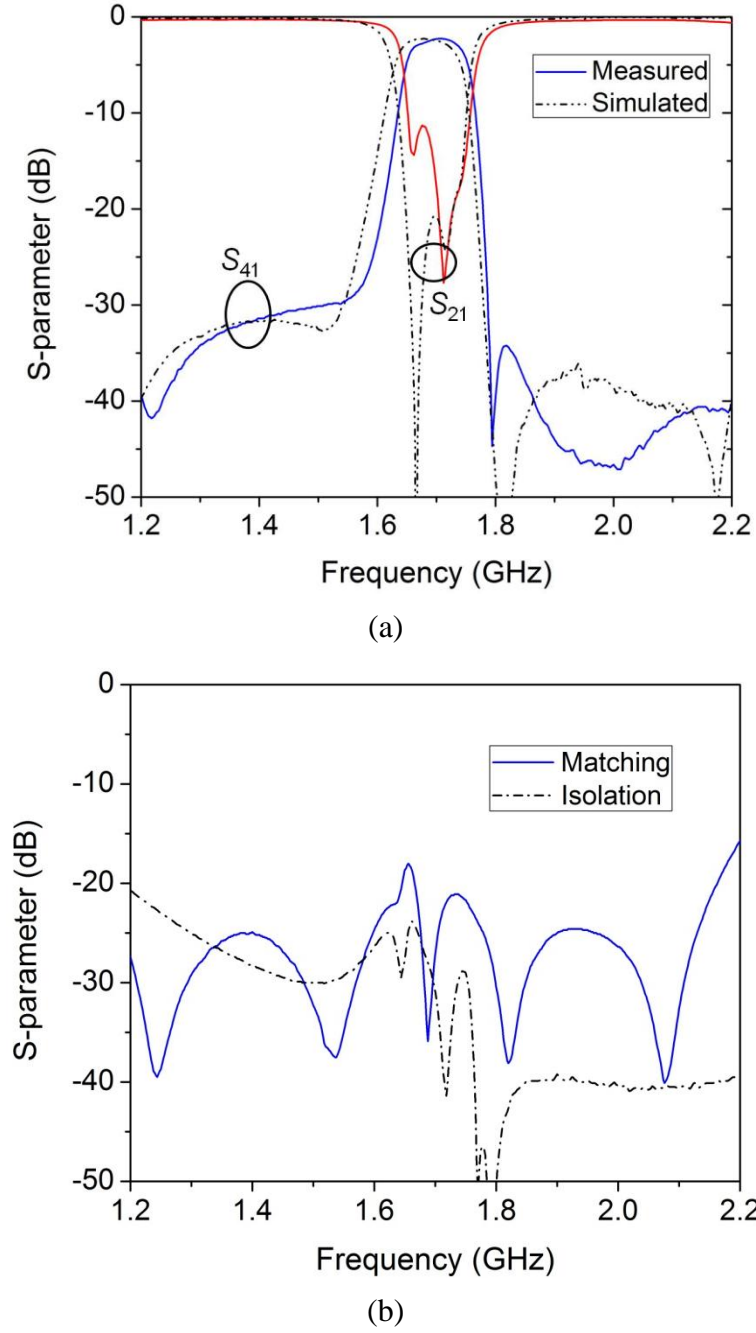


Figure 6.5 The simulated and measured S_{41} and S_{21} response of the DF prototype (a), and its measured matching and isolation performance (b).

part has two unit cells, and consists of three series capacitors and two shunt inductors, as also shown in the Figure 6.4. The shunt inductance consists of two 2.2nH inductors and a 3.3mm shorted stub connected in series. The series capacitors at the two ends consist of one 2.2pF and

one 2.4pF capacitor in parallel, and the capacitor in the center is 2.2pF. This CRLH TL is designed to achieve phase-matching with the corresponding 130° microstrip line.

The band-pass S_{41} response and the band-stop S_{21} response of the DF from 1.2 to 2.2 GHz are shown in Figure 6.5(a) where solid lines are measured results and dotted line is simulated results. The insertion loss at 1.7GHz is about 2.4dB. By comparing to the designed BRF response in Figure 6.3, we can see that the zeros at 1.8GHz and the sharp cut-off in the S_{11} of the BRF are preserved in the S_{41} of the DF. However, the band-reject level in S_{21} of the DF is only about 10dB, higher than the simulated case. This is possibly due to the manufacturing tolerance, the lumped element value variation and extra loss introduced by the lumped elements. Notice that the out-of-band rejection level of S_{41} is comparable to the designed BRF response over 1.2~2.2GHz. This validates the merit of adapting this direct coupled BRF structure for high order directional filter realization. The S_{11} and S_{31} are shown in Figure 6.5(b). For clarity, only measured responses are shown. Wide-band matching and isolation are achieved, which is the typical characteristic of the DF.

Notice that there are extra even-mode matching circuits being added at the two sides of the mirrored BRF, as indicated in Figure 6.4. It consists of three 10nH inductors in series at the two ends, connected by a transmission line close to 180° . It has been pointed out that the out-of-band rejection level of S_{41} will be affected by the matching of the mirrored BRF under even-mode excitation. Since the rejection level we are realizing is deep (~ 35 dB), extra care is taken by adding the matching circuits to improve the even-mode matching to be better than 30dB without disturbing the odd-mode operation.

6.4 CONCLUSION

This Chapter, we demonstrated that by using direct-coupled BRF prototype in the DF design, we can avoid the deviation of DF performance from the designed BRF happening at frequencies too close to the center frequency, and we can incorporate the CRLH phase-matching easily for better isolation performance. The prototype demonstrated a 4-pole DF with CRLH phase-matching. This is the highest order of DF reported using $\lambda/2$ resonator structure, yet it is 30% smaller than the 3-pole elliptic DF Chapter 5. With even-mode matching circuits, the stop-band rejection is about 30dB in the lower frequency and 35dB in the higher frequency.

6.5 BIBLIOGRAPHY

- [6.1] J. D. Rhodes, "Waveguide bandstop elliptic function filters," *IEEE Trans. Microwave Theory & Tech*, vol. 20, no. 11, pp. 715-718, 1972.
- [6.2] R. J. Cameron, M. Yu, Y. Wang, "Direct-coupled microwave filters with single and dual stopbands," *IEEE Trans. Microwave Theory & Tech*, vol. 53, no. 11, pp. 3288-3297, 2005.